Physics – Uspekhi **65** (5) 421 – 439 (2022)

REVIEWS OF TOPICAL PROBLEMS PACS numbers: 03.67.Lx, 03.75.Lm, 42.50.Dv, 85.25.Cp

State control in superconducting quantum processors

V A Vozhakov, M V Bastrakova, N V Klenov, I I Soloviev,
W V Pogosov, D V Babukhin, A A Zhukov, A M Satanin

DOI: https://doi.org/10.3367/UFNe.2021.02.038934

Contents

Abstract. The review elucidates recent advances in the development of superconducting qubits and quantum circuits designed for a new generation of quantum processors. It primarily focuses on the analysis of control methods for multi-qubit systems — multi-particle quantum systems with configurable — including in situ — parameters of individual elements and connections between them. It is shown how solving fundamental physical problems in this area (for example, the interaction of an artificial atom with strong and short field pulses) allows increasing the efficiency of existing quantum processors when implementing specific algorithms.

V A Vozhakov [1, a], **M V Bastrakova** [2, b], **N V Klenov** [1, 3, c], **I I Soloviev** [1, 2, d], **W V Pogosov** [4, e], **D V Babukhin** [4, f], **A A Zhukov** [4, g], **A M Satanin** [4, 5, h]
[1] Lomonosov Moscow State University, Leninskie gory, 119991 Moscow, Russian Federation
[2] National Research Lobachevsky State University of Nizhni Novgorod, prosp. Gagarina 23, 603022 Nizhny Novgorod, Russian Federation
[3] Moscow Technical University of Communications and Informatics, ul. Aviamotornaya 8a, 111024 Moscow, Russian Federation
[4] Dukhov Research Institute of Automatics, ul. Sushchevskaya 22, 119017 Moscow, Russian Federation
[5] National Research University Higher School of Economics, ul. Myasnitskaya 20, 101000 Moscow, Russian Federation
E-mail: [a] sevozh@yandex.ru, [b] marina_vd@mail.ru, [c] nvklenov@gmail.com, [d] igor.soloviev@gmail.com, [e] Walter.Pogosov@gmail.com, [f] dv.babukhin@physics.msu.ru, [g] zugazoid@gmail.com, [h] asatanin@gmail.com

Received 8 December 2020, revised 11 February 2021
Uspekhi Fizicheskikh Nauk **192** (5) 457 – 476 (2022)
Translated by V L Derbov

Keywords: quantum operations, superconductivity, Josephson effect, quantum algorithms

1. Introduction

Superconducting quantum bits (qubits) and processors based on them are a subject of large-scale investigations, since they are potentially capable of accelerating the solution to computationally complex problems arising in simulations of multi-particle quantum systems and the analysis of problems in quantum chemistry, materials science, etc. [1–5].

The processors under consideration operate with evolving state amplitudes of elements of quantum electrodynamic (QED) circuits consisting of superconducting lines and qubits. To understand the processes that occur in such circuits, it is reasonable to address the known analogy with using electronic circuits in the study of nuclear collisions [6]: in a configurable and controlled quantum 'multi-particle' system [7], the collisions of excitations, causing quantum correlations in the finite register states, are simulated.

The classification of superconducting qubit types is based on comparing characteristic values of the electrostatic and Josephson energies. Within this approach, it is possible to construct a table analogous to the periodic table of elements [8]. Of primary interest are the charge [9, 10], flux [11, 12], and phase [13, 14] qubits, quantronium [15], fluxonium [16], and transmon [17].

Presently, many research teams all over the world are busy creating multi-qubit 'superconducting' processors, but the most advanced in developing noisy intermediate-scale quantum (NISQ) processors are the laboratories of IBM, Google, Intel, and Rigetti Computing. All these research groups use transmons as basic elements. Each of the above companies

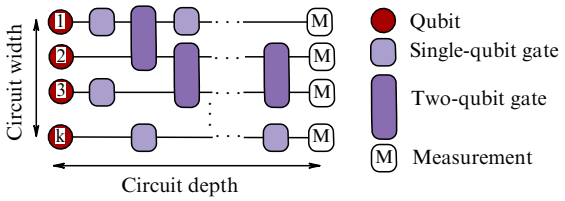

Figure 1. (Color online.) Illustration of the notions of width and depth of a quantum circuit. Notation used for qubits and operations is introduced in the figure.

has managed to create at least one working multi-qubit quantum processor and to demonstrate with it the possibility of implementing one quantum algorithm or another. The processors differ in the number and topology of qubits, as well as in the implementation of interqubit connections based on QED circuits with the possibility of addressed control of the processor elements.

The main problems with modern quantum processors are the limited lifetime of qubit coherent states and the consequent limitation of the number of logical operations (gates) transforming the state of the system. These problems can be partially solved by using specially developed correction algorithms, but these require additional operations and additional qubits.

A number of researchers managed to overcome the technological problems that recently seemed unresolvable and create qubits with a decoherence time of up to 100 μs, as well as high-Q resonators for readout of the qubit states [7]. To date, the 'noisiness' of quantum registers has not been completely removed; therefore, for comparing with classical computers in order to demonstrate the 'quantum supremacy,' a specially chosen algorithm was used, which allowed generating a semblance of a random sequence with prescribed specific features. The Sycamore quantum computer solved the problem in 200 s, which is beyond the capabilities of modern classical supercomputers.

In this context, the *width* and the *depth* are characteristics of quantum circuits important for comparing the capabilities of various processors. The circuit width is the number of all qubits of the system and the circuit depth is the number of gate operations performed before the moment of measurement, i.e., the destruction of the qubit state (Fig. 1). The circuit width is limited only by the processor architecture (the number of fabricated qubits), whereas the maximal depth of the circuit depends on the magnitude of external noises, to wit

$$\text{wid} \times \text{dep} \ll \frac{1}{P_{\text{err}}}\,, \tag{1}$$

where wid is the circuit width, dep is the circuit depth, and P_{err} is the error probability.

To evaluate the capabilities of a quantum computer, the IBM team proposed a notion of *quantum volume* — a quantity equal to $2^{X_{\text{Q}}}$, where X_{Q} is both the depth and the width of a circuit at which the given algorithm can be executed. The problem of optimizing this quantity in superconducting computational NISQ systems is a subject of primary interest of the present review.

The design and physical implementation of qubits, as well as connecting paths and control devices (gates), will be presented relatively briefly in this review. We focus on analyzing the problems of controlling multi-particle quantum systems and describing ways to increase the efficiency of existing quantum processors and increasing their quantum volume. First, we will consider the reasons limiting the circuit depth. Second, we will analyze the construction of the most promising qubit types and then the physical implementation of operations with superconducting qubits. Finally, we will discuss the possibilities of improving the methods of 'quantum control.'

2. Quantum processor elements

2.1 Qubit model

For a number of reasons (long decoherence time, scalability, fast control), transmons are considered the most promising type of superconducting qubit used to date. Transmons were first described in Ref. [17], their physical implementation being based on superconducting islands separated by a thin layer of dielectric. In order to reduce the noise impact, transmons have a large capacitance connected between the islands, making the qubit charging energy substantially less than the Josephson energy. This localizes the phase, so, the lower energy levels of the Josephson nonlinear oscillator can be considered a qubit. To control the Josephson energy and the distance between the energy levels, a two-junction superconducting quantum interference device (SQUID) is commonly used as a nonlinearity, whose Josephson energy $E_{\text{J}} = I_{\text{c}}\Phi_0/(2\pi)$ substantially exceeds the charging energy $E_C = e^2/(2C)$. Here, I_{c} is the critical current of the Josephson junction, C is the junction capacitance, Φ_0 is the magnetic flux quantum, and e is the electron charge. This type of basic element of a quantum computer evolved from a single-junction charge qubit [14]. The Hamiltonian of a transmon has the form

$$\hat{H}_0 = 4E_C(\hat{n} - n_{\text{g}})^2 - E_{\text{J}}\cos\hat{\phi}\,, \quad [\hat{\phi}, \hat{n}] = \text{i}\,, \tag{2}$$

where $n_{\text{g}} = Q_{\text{r}}/(2e) + C_{\text{g}}V_{\text{g}}/(2e)$ is the effective displaced charge in the units of Cooper pair charge $2e$ controlled by the voltage V_{g} at the gate electrode with the capacitance C_{g}, Q_{r} is the displaced charge induced by the environment, and ϕ is the Josephson phase of the junction.

The Schrödinger equation with Hamiltonian (2) is exactly solvable using the special Mathieu functions for any ratio E_C/E_{J}, the energy levels $E_n(n_{\text{g}})$ as functions of the displaced charge n_{g} being characterized by a strong dispersion. If the condition $E_C \ll E_{\text{J}}$ is satisfied, the 'straightening' of the dispersion characteristic (the energy of levels vs the charge) occurs, decreasing the noise impact on the qubit state due to the lessening of the charge fluctuations on the gate and the substrate. For a long time, the charge noise was a great problem for charge qubits. At first, the decoherence time did not exceed 1 μs [17].

Let us explain in more detail what we are talking about. When $E_C \ll E_{\text{J}}$, the phase is strongly localized; therefore, in expression (2), the expansion can be performed:

$$\cos\hat{\phi} = 1 - \frac{\hat{\phi}^2}{2!} + \frac{\hat{\phi}^4}{4!} + \ldots\,.$$

By introducing the creation $\hat{a}^\dagger$ and annihilation $\hat{a}$ operators, we make it possible to perform the parameterization

$$\hat{n} = \text{i}\left(\frac{E_{\text{J}}}{16E_C}\right)^{1/4}(\hat{a} - \hat{a}^\dagger)\,, \qquad \hat{\phi} = \left(\frac{2E_C}{E_{\text{J}}}\right)^{1/4}(\hat{a} + \hat{a}^\dagger)$$

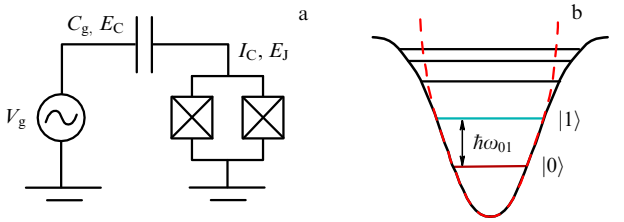

Figure 2. Schematic of a transmon (a) and its potential energy together with the energy spectrum of stationary states (b).

and to disregard the dependence of energy levels on n_g. In such an approximation, the transmon can be considered a nonlinear oscillator having a nonequidistant energy spectrum with the anharmonicity parameter $\omega_\alpha = \omega_{01} - \omega_{12}$, where the transition frequencies $\omega_{nm} = (E_m - E_n)/\hbar$ are determined by the proportion of energies E_J and E_C (Fig. 2). The frequency of the transition between the ground state and the first excited state $\omega_{01} = (E_1 - E_0)/\hbar$ determines the frequency of the effective qubit excitation by electromagnetic Rabi pulses with the carrier frequency close to ω_{01}. Figure 2 emphasizes that the external field acts on the qubit through the capacitive coupling to the waveguide path:

$$\hat{H} = \hat{H}_0 - \frac{8E_C C_g}{2e}\,\hat{n}V_g\,. \tag{3}$$

Therefore, the full Hamiltonian of the qubit in the presence of external action can be presented as

$$\hat{H} = \omega_{01}\hat{a}^\dagger\hat{a} + \omega_\alpha(\hat{a} + \hat{a}^\dagger)^4 - \mathrm{i}\varepsilon(t)(\hat{a} - \hat{a}^\dagger), \tag{4}$$

where $\varepsilon(t)$ is the envelope of the acting field, $\omega_{01} = \sqrt{8E_J E_C}/\hbar$, $\omega_\alpha = -E_C/(12\hbar)$.

Upon the condition of anharmonicity $E_C \leqslant E_J$, the qubit Hamiltonian can be written in the two-dimensional Fock subspace $|0\rangle$ and $|1\rangle$, where $\hat{a}^\dagger\hat{a}|n\rangle = n|n\rangle$, which is convenient to express in terms of the Pauli matrices σ_x, σ_y, and σ_z:

$$H = -\frac{\omega_{01}}{2}\,\sigma_z + \varepsilon(t)\sigma_y\,. \tag{5}$$

For the basis states, the spinors

$$|0\rangle = \begin{pmatrix}1\\0\end{pmatrix}, \quad |1\rangle = \begin{pmatrix}0\\1\end{pmatrix}$$

can be chosen and the wave function of the qubit can be presented in the form

$$|\Psi_t\rangle = \alpha(t)|0\rangle + \beta(t)|1\rangle\,, \tag{6}$$

where α and β are complex coefficients, $|\alpha|^2 + |\beta|^2 = 1$.

The anharmonicity characteristic ω_α for a typical transmon amounts to 3–5% of the qubit frequency; therefore, when the excitation is strong, it is necessary to extend the subspace by including into consideration the next stationary state $|2\rangle$, to which 'leakage' is possible. In Ref. [18], it is shown that the qubit model in the form of a two-level system cannot provide sufficient accuracy for calculating the dynamics of the qubit states under the action of controlling pulses.

For qubit state (6), a simple geometric interpretation is introduced representing it by a point on the Bloch sphere with

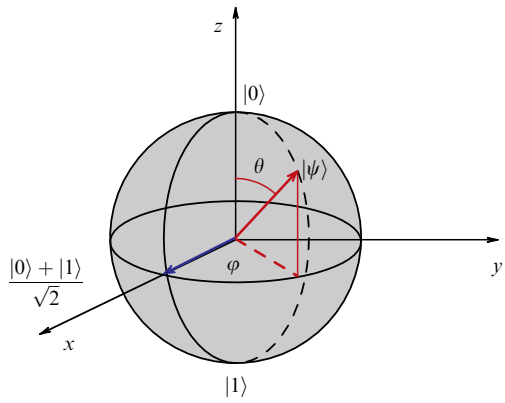

Figure 3. (Color online.) Graphic representation of the qubit state (Bloch sphere).

the unit radius (Bloch–Redfield model). The complex coefficients α and β determine the state vector and, with normalization and the arbitrary phase taken into account, can be parameterized as

$$\alpha = \cos\frac{\theta}{2}\,, \quad \beta = \exp(\mathrm{i}\varphi)\sin\frac{\theta}{2}\,, \tag{7}$$

where φ is the azimuthal angle and θ is the polar angle that determine the geometric position of the point (Fig. 3).

Such an interpretation allows choosing the basis of two vectors: $|0\rangle$ codirectional with the z-axis ($\theta = 0$) and $|1\rangle$ having the opposite direction ($\theta = \pi$). Thus, any operation can be represented as a rotation around three independent axes in the spin space moving a point on the Bloch sphere from one position to another.

Ideal operations always occur on the surface of the Bloch sphere, but in reality the influence of environment leads to blurring of this picture, and the qubit state finds itself inside the Bloch sphere. This process greatly affecting the control of quantum systems is called decoherence.

2.2 Noises in qubits

In the Bloch–Redfield model, two processes of the noise effect on a qubit are distinguished: relaxation and dephasing. Relaxation is the process of spontaneous transition of a qubit from the state $|1\rangle$ to the state $|0\rangle$ during time T_1, called the relaxation time. The maximal possible relaxation time of a superconducting qubit is limited by the Purcell effect [19]. Dephasing is the process of destruction of the qubit superposition state $(1/\sqrt{2})(|0\rangle + |1\rangle)$ during dephasing time T_2.

The processes of relaxation are presented on the Bloch sphere through motion along the z-axis, and this process is irreversible. Dephasing can consist of relaxation or 'pure dephasing' — the motion in the xy plane with the characteristic time of pure dephasing T_φ. The total time of destruction of a superposition state is determined as

$$\frac{1}{T_2} = \frac{1}{T_\varphi} + \frac{1}{2T_1}\,. \tag{8}$$

Decoherence processes can be described as interactions of the qubit with a bosonic reservoir. In such a model, the process of interaction can be considered Markovian and the dynamics of the density operator of the qubit can be calculated using the equation for the density matrix operator

in the Lindblad form [20, 21]:

$$\frac{\partial\rho}{\partial t} = -\mathrm{i}[\rho, \bar{H}] + \Gamma_\varphi(\sigma_z\rho\sigma_z - \rho) + \frac{\Gamma_1}{2}(2\sigma_-\rho\sigma_+ - \sigma_+\sigma_-\rho - \rho\sigma_+\sigma_-)\,. \tag{9}$$

Here, the parameter $\Gamma_\varphi = 1/(2T_\varphi)$ characterizes the rate of the pure dephasing process, and the parameter $\Gamma_1 = 1/T_1$ is similarly responsible for the relaxation rate, $\sigma_\pm = (\sigma_x \pm \mathrm{i}\sigma_y)/2$. For numerical calculations, it is convenient to present the density matrix in the form

$$\rho = \begin{pmatrix} \rho_{00} & \rho_{01} \\ \rho_{10} & \rho_{11} \end{pmatrix} = \frac{1}{2}(\mathbb{I} + \boldsymbol{\sigma}\mathbf{R})\,,$$

where $\mathbb{I}$ is the unit matrix, $\boldsymbol{\sigma}$ is the set of Pauli matrices. Equation (9) for the density matrix is equivalent to the system of equations for the components of vector $\mathbf{R} = \mathrm{Tr}\,(\boldsymbol{\sigma}\boldsymbol{\rho}(t))$:

$$\begin{cases} \dot{R}_x = -\omega_{01}R_y - 2\varepsilon(t)R_z - \dfrac{1}{2}\Gamma_1 R_x - 2\Gamma_\varphi R_x\,, \\ \dot{R}_y = \omega_{01}R_x - 2\Gamma_\varphi R_y - \dfrac{1}{2}\Gamma_1 R_y\,, \\ \dot{R}_z = 2\varepsilon(t)R_x - \Gamma_1 R_z - \Gamma_1\,. \end{cases} \tag{10}$$

Let us present the relaxation processes in terms of the dynamics of vector $\mathbf{R}(t)$ on the Bloch sphere (Fig. 4). Let the qubit be prepared in the state $|\Psi\rangle = (1/\sqrt{2})(|0\rangle + |1\rangle)$ at the initial moment of time. In the absence of external excitation ($\varepsilon(t) = 0$), the qubit will relax to the ground state during the time T_1, $\rho_{11}(t) = \rho_{11}(0)\exp(-t/T_1)$. In Fig. 4a, the points on the sphere show the motion trajectory of the Bloch vector, as well as the evolution of the element ρ_{11} of the density matrix. According to Eqn (10), the dephasing processes are expressed in terms of the off-diagonal elements of the density operator matrix and lead to a phase disturbance of the qubit wave function. Due to the energy conservation law, the diagonal elements of the density operator matrix will be preserved, and the Bloch vector will rotate in the xy plane (Fig. 4b). This can be interpreted as a stochastic trembling of phase φ in expression (7).

To reduce the effect of environment-induced noises on a qubit, it is necessary to clarify what physical processes are responsible for decoherence. Note that the modification of a charge qubit to a transmon allowed getting rid of the negative effect of charge noise, which was considered in Section 2.1; therefore, the charge noise will not be discussed below.

2.2.1 Flux noise. The reason for the appearance of flux noise is the stochastic variation of spin polarization and, as a consequence, of a magnetic dipole moment of molecules on the superconductor surface. Experimental studies [22] have shown that the main source of the flux noise in thin superconducting films is adsorbed molecular oxygen O_2. The flux noise can be reduced by using a higher vacuum in the course of qubit fabrication, surface passivation with ammonia molecules, and ultraviolet (UV) exposure [23]. The main method of removing this problem is a transition (by choosing the qubit parameters) to the state, which ensures minimum sensitivity to the flux noise.

2.2.2 Photon noise. Residual fields in the resonator give rise to fluctuations in the number of photons, which affect the qubit

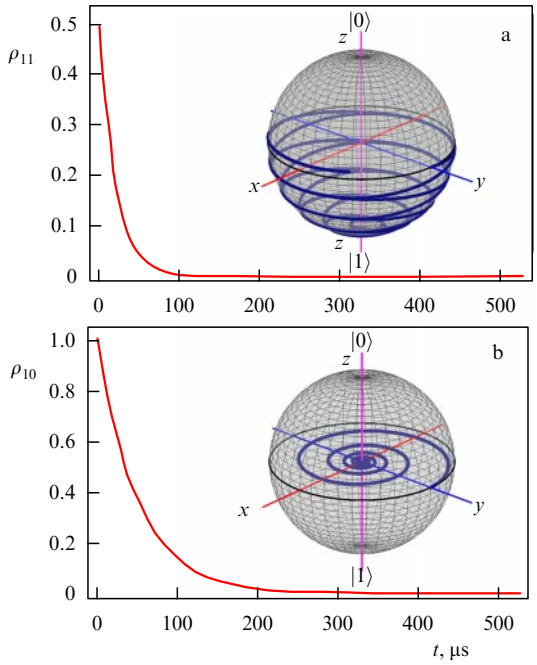

Figure 4. (Color online.) Dissipative dynamics of the qubit state $(1/\sqrt{2})(|0\rangle + |1\rangle)$ under (a) relaxation Γ_1 ($\Gamma_\varphi = 0$), (b) dephasing Γ_φ ($\Gamma_1 = 0$).

state and shift the resonance frequency in the 'qubit + resonator' system due to the Stark effect [24]. The photon noise is the dominant dephasing mechanism in superconducting qubits, especially in the state, providing the minimum sensitivity to flux noise.

2.2.3 Quasiparticle poisoning. In addition to a supercurrent, nonequilibrium quasiparticles can also pass through a tunnel contact, namely, nonpaired electrons that negatively affect the qubit operation and reduce both the relaxation and the dephasing time. Quasiparticles arise because of breaking Cooper pairs due to thermal fluctuations, external electromagnetic radiation, and interaction with electrons, their concentration exponentially falling with a decrease in temperature and being of the order of $10^{-7}-10^{-6}$ per Cooper pair in modern transmons. Quasiparticles affect not only the qubit state but also the efficiency of the resonator operation; therefore, it is of primary importance to eliminate their influence. There are several methods to fight against quasiparticle poisoning: flux traps [25], pumping-off pulses [26], traps of normal metal [27], and superconducting traps [28].

2.2.4 Radiation noises. External noises caused by background radiation are inevitably present in the laboratory equipment and walls, while noises caused by cosmic radiation flows can be an additional obstacle on the way towards a further increase in the decoherence time and usage of error correction codes. The fact of the radiation effect on qubits was demonstrated in Ref. [29]. Using a controlled source of ionizing radiation (a copper film containing the ^{64}Cu isotope), the authors of Ref. [29] exposed to radiation an aluminum qubit on a silicon substrate and found the dependence of the superconducting state decay rate (i.e., the rate of quasiparticle generation) on the source intensity. As is known, cosmic rays come from the atmosphere with high energies [30]. For

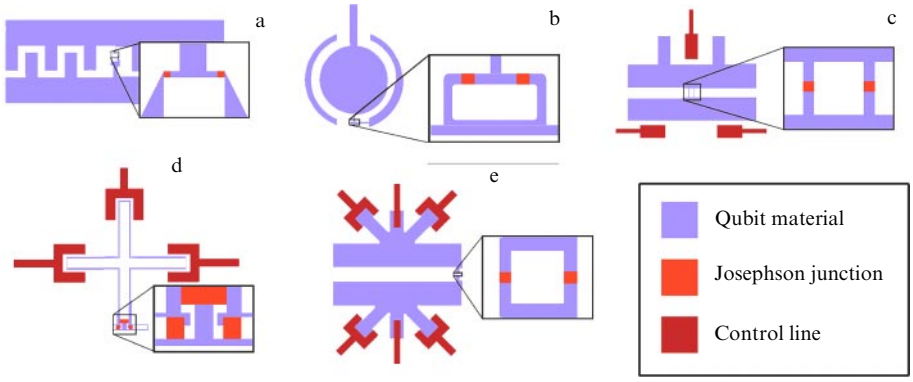

Figure 5. (Color online.) Schematic of the basic transmon technologies used. Superconducting metal is shown in lilac, Josephson junction, in orange, element of control and readout lines, in red. (a) Classical transmon. (b) Concentric transmon. (c) IBM transmon. (d) Xmon. (e) Starmon.

example, high-energy muons (average energy of 460 keV) or gamma rays (energy of 1 MeV) can give rise to cascades of phonon creation reactions in a superconductor, which, in turn, can break Cooper pairs and create quasiparticles until their energy is equal to the superconducting gap [31]. Due to the cascade processes, large-scale charge fluctuations will arise in the superconductor, which can hamper the correction of errors induced by noises of this kind. In this case, it becomes important to find new methods of shielding superconducting registers against radiation [32, 33]. In particular, applying a film of a narrow-gap superconductor or normal metal on the qubit will allow partial collection of phonons generated by the radiation in the shielding film and their deflection from the active qubit region [31].

2.3 Topology of qubits

2.3.1 Classical transmon. The first transmon technology developed [7] was not oriented toward solving a particular computation problem. It was a Cooper pair box (CPB) of two superconducting islands, the space between which forms a line of a 'snake' shaped resonator that allows shunting two Josephson junctions with an additional capacitance of these islands (Fig. 5a). A drawback of this design is the extremely short relaxation time, even with a good quality of fabrication (≈ 1.5 μs). When developing this topology, the problem of studying connections between qubits was not formulated, so that using such transmons to create a multiqubit processor does not seem possible.

2.3.2 Concentric transmon. In 2018, Rigetti et al. [34] described the design of a 'concentric' transmon with increased relaxation time. Two superconducting electrodes form the central island with the shape of a circle and a concentric ring surrounding it. These electrodes, connected by two Josephson junctions, form a gradiometric superconducting interferometer (Fig. 5b). Such a design reduces the sensitivity of the transmon to flux noise, the Purcell effect, and quasiparticle poisoning due to the 'smoothing' of the transmon topology, which reduces the probability of defects appearing at the edges. Moreover, the design considered allows forming a rather high number of interqubit connections and current-carrying paths for the control and readout system.

2.3.3 IBM transmon. IBM [35–37] also resorted to limiting the possibilities of tuning the qubit spectrum in order to reduce the sensitivity to flux noise. IBM qubits are tuned to one excitation frequency, which allows achieving a relaxation time up to 100 μs, since there are no mechanisms of transmon interaction with noises at other frequencies. The transmon in such an engineering solution consists of two superconducting islands connected by two Josephson junctions (Fig. 5c). An obvious disadvantage of such a design is the impossibility of controlling the qubit parameters.

2.3.4 Xmon. When creating the Xmon [38], the primary tasks were to implement the module principle and to simplify the methods of connection between the qubits. The Xmon top view is a four-ended cross (X). Each of the four 'arms' of the qubit is connected to a separate element: a readout resonator (Fig. 5d), other qubits, and a system of microwave XY control and flux Z control. The cross is also a shunting capacitance of the transmon connected to the main interferometer. The Xmon circuit is equivalent to the transmon, with the only difference being that the Xmon is grounded, which makes it possible to avoid the parasitic effect of residual fields and charges. The connection in a system of Xmons is achieved by allocating a certain function to each 'arm'; the role of each 'arm' can be changed and more than one function can be assigned to each 'arm', so that each connection is easy to implement and optimize. The transmon design can be additionally varied by changing the capacitor shape.

2.3.5 Starmon. The starmon developed by a research team at the Intel Corporation [39] is another popular topological solution that received particular recognition in the design of surface code systems. The starmon is a modification of the transmon (Fig. 5e). As a rule, it has seven ports. Four of them are connected with neighboring starmons, the fifth one is used for XY control by microwave pulses, the sixth one is used for Z control by a magnetic flux, and the seventh one is for connecting the starmon to the readout resonator (on the whole, these connections are similar to those in Xmons). This modification is useful for making a processor with a large number of interqubit connections.

Thus, it is possible to formulate two basic criteria for choosing the transmon topology: the possibility of a connection with other qubits and the resistance of the chosen topological solution to flux noise. There are papers on the study of the dependence of the generated flux noise on the qubit geometric size [40]. To reduce the sensitivity to flux noise, thicker wires, thicker films, and a perimeter of the

superconducting ring as small as possible are required [41, 42].

3. Operations in a quantum processor

3.1 Basic types of operations

Quantum logic gates (including control of the state amplitudes of QED circuit elements) are fundamentally different from classical ones. The number of inputs and outputs in quantum logic gates must coincide, because in quantum calculations all operations are reversible. A mathematical description of quantum logic gates is possible in terms of unitary matrices in a Hilbert space. The basic operations used in practice are one-qubit and two-qubit, but there are also operations using the entangled states of three or more qubits [43–45]. Reducing both the number of errors and the duration of a gate operation is important in order to increase the quantum control efficiency and the processor quantum volume.

The one-qubit operations most frequently used in algorithms are the rotations of the qubit state on the Bloch sphere by 180° around the axes (X-, Y-, and Z-gates), the rotation of a state by 90° along the z-axis (S-gate), and the transition to a superposition state (Had-gate, or Hadamard gate). There is also the operation of an arbitrary rotation of the Bloch sphere (Phase).

The operation of inverting the populations of the basis states corresponds to the operator

$$C_{\mathrm{NOT}} = \begin{pmatrix} 0 & 1 \\ 1 & 0 \end{pmatrix}.$$

The Hadamard operator

$$C_{\mathrm{Had}} = \frac{1}{\sqrt{2}} \begin{pmatrix} 1 & 1 \\ 1 & -1 \end{pmatrix}$$

corresponds to the transition of a qubit to the superposition state with equal populations of energy levels.

Among the two-qubit operations of interest are those leading to the entanglement of states. In particular, the gates CNOT (Controlled NOT) and CZ (Controlled Z) are implement by one-qubit NOT and Z gates, depending on the state of the controlling qubit (CX, CY, etc. are introduced similarly). As in classical logic, there is a universal set of gates, using which it is possible to reproduce any algorithm. The CNOT and Phase are examples of such a set. Let us dwell on the implementation of one- and two-qubit operations in the multi-particle systems considered.

3.2 Single-qubit operations

For superconducting quantum processors, an arbitrary rotation of the Bloch vector can be implemented by control electromagnetic pulses with the frequency close to the qubit frequency. This method of control was called the 'Rabi technique,' and the effect of the applied electromagnetic field (5) can be expressed as

$$\varepsilon(t) = A_{\mathrm{R}} \cos(\omega_{\mathrm{R}} t), \tag{11}$$

where A_{R} is the amplitude, $\omega_{\mathrm{R}} = \omega_{01} + \delta\omega$ is the pulse frequency, and $\delta\omega$ is the small detuning from the exact resonance, $\delta\omega \ll \omega_{01}$. The analytical description of qubit dynamics in the field of a Rabi pulse is based on the resonance perturbation theory (Rabi approximation) [20, 46]. Under this action, the qubit energy level populations oscillate at the Rabi frequency $\Omega = ((\delta\omega)^2 + A_\Omega^2)^{1/2}$, where $A_\Omega = (A_{\mathrm{R}}/\hbar)\,\langle 0|\sigma_x|1\rangle$, and for the ground state the population depends on time as

$$W_0(t) = 1 - \frac{A_\Omega^2}{\Omega^2} \sin^2\left(\frac{\Omega t}{2}\right). \tag{12}$$

The required duration of a Rabi pulse is $(100-1000)T$, where $T = 2\pi/\omega_{\mathrm{R}}$, the particular value being chosen depending on the operation type. By solving Eqn (12) numerically, it is possible to determine the durations and amplitudes of the control pulses for implementing the required quantum operations [47]. At zero detuning, $\delta\omega = 0$, and an arbitrary envelope of the Rabi pulse, the moment it is switched off is determined by the integral of the envelope over time — 'the area law.'

Figure 6 shows the evolution of the qubit ground state under the action of Rabi pulses (12) in the case of implementing the NOT and Had gates, according to the numerical solution of Eqn (9). Note that, for the characteristic transmon frequency within the range from 1 to 10 GHz, the time of executing quantum logical operations is from a few tens to a few hundred nanoseconds.

3.3 Microwave implementation of single-qubit operations

Practically, for controlling qubit states, RF analog quadrature mixers (I/Q mixers) are used. The signal applied to the

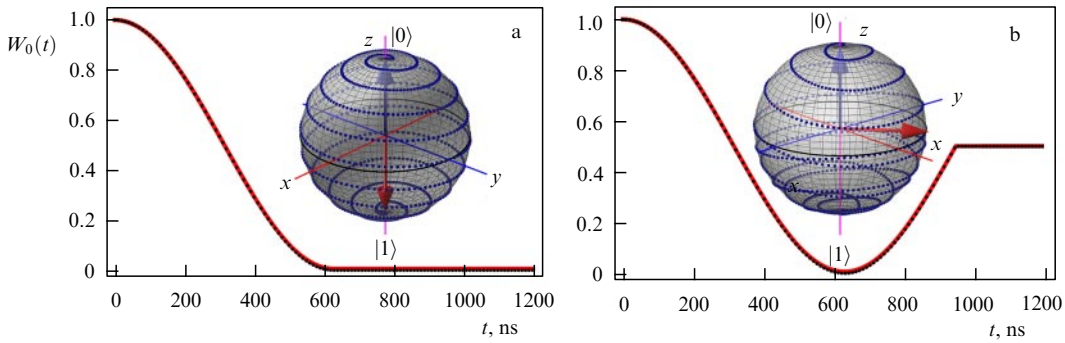

Figure 6. (Color online.) Evolution of qubit ground state population W_0 under the action of a Rabi pulse when implementing the NOT (a) and Hadamard (b) quantum operations (black dots correspond to the result of the analytical calculation using Eqn (12), red solid line, to the result of numerical modeling (9) with the Hamiltonian (5)). Insets schematically show the evolution of the state vector on the Bloch sphere. Parameters of the qubit and the pulses are $\omega_{01}/(2\pi) = 5$ GHz, $E_C/E_{\mathrm{J}} = 0.25$, $A_{\mathrm{R}} = 0.23$ GHz, $\delta\omega/(2\pi) = 0.0013$ GHz, $T_\varphi = 100$ μs.

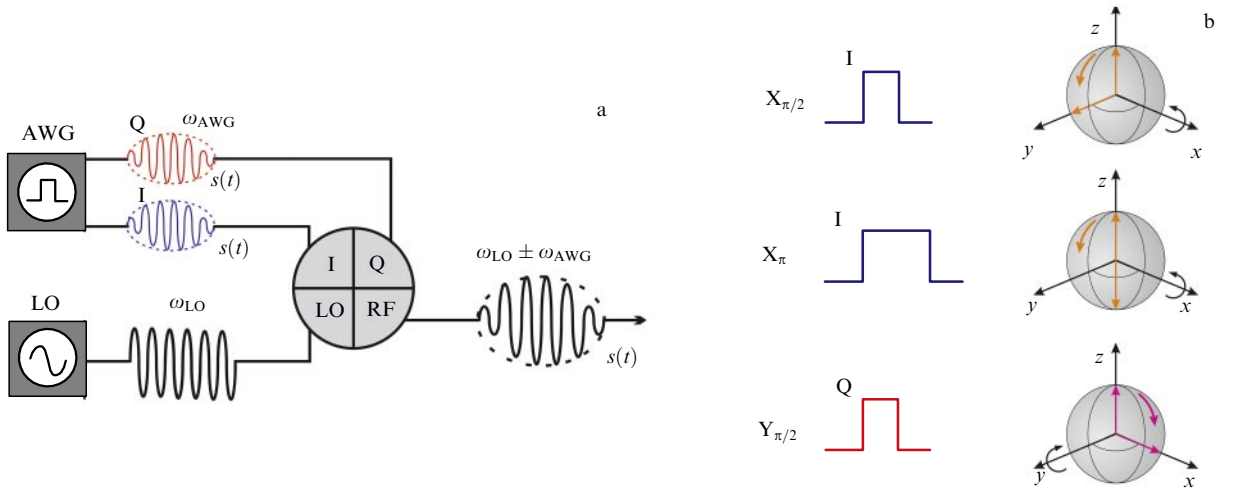

Figure 7. (Color online.) Using a quadrature modulator for pulse generation. (a) Schematic diagram of connecting generators to the modulator. AWG — arbitrary waveform generator, RF — radiofrequency generator. (b) Schematic representation of gate pulses of voltage and the result of their action on the qubit state, presented on Bloch spheres.

modulator arrives at the local oscillator (LO) port and is multiplied by the signals at the in-phase (I) and quadrature (Q) ports with the phase difference of $\pi/2$. Thus, the modulated control signal is obtained with the possibility of switching to a constant continuous signal. The schemes implementing the basic operation signals for the qubit are shown in Fig. 7. To obtain the voltage signal $V_{\mathrm{d}}(t)$ of an arbitrary shape, an appropriate generator is used.

It can be shown that such a method of control implies only rotations about the x- and y-axes. Indeed, in the Bloch–Redfield model, a qubit affected by the control voltage $V_{\mathrm{d}}(t)$ corresponds to the Hamiltonian

$$H = -\frac{\omega_{01}}{2}\,\sigma_z + n_C V_{\mathrm{d}}(t)\left[\cos\left(\omega_{01}(t)\right)\sigma_y - \sin\left(\omega_{01}(t)\right)\sigma_x\right], \tag{13}$$

where n_C is the value of fluctuation charge normalized to the capacitance of the system.

However, in this way, it is also possible to perform rotations around the z-axis by an arbitrary angle φ_0. For this purpose, it is necessary to execute a rotation through the angle θ around the x-axis and then a similar rotation, but around the axis inclined at the angle φ_0 relative to the first operation:

$$\begin{aligned} X_\theta^{(\varphi_0)} X_\theta &= \exp\left[\frac{\theta}{2}\left(\cos(\varphi_0)\sigma_y - \sin(\varphi_0)\sigma_x\right)\right] X_\theta \\ &= Z_{-\varphi_0} X_\theta Z_{\varphi_0} X_\theta\,. \end{aligned} \tag{14}$$

The qubit state readout implies projecting on the z-axis, so that the last operation $Z_{-\varphi_0}$ will not affect the result. Such an approach is referred to as 'virtual Z-gate' [48].

3.4 Flux implementation of single-qubit operations

Another way of executing Z-operations is based on using a separate control magnetic flux line. To this end, consider a qubit, in which two Josephson junctions form a SQUID. Let us make use of the fact that the Josephson energy of the qubit included in the Hamiltonian depends on the difference between the Josephson energies of the junctions $d = (E_{\mathrm{J2}} - E_{\mathrm{J1}})/(E_{\mathrm{J2}} + E_{\mathrm{J1}})$ and the magnetic flux Φ [17]:

$$E_{\mathrm{J}}(d, \Phi) = (E_{\mathrm{J1}} + E_{\mathrm{J2}})\cos\left(\frac{\pi\Phi}{\Phi_0}\right)\sqrt{1 + d^2\tan^2\left(\frac{\pi\Phi}{\Phi_0}\right)}\,. \tag{15}$$

From the point of view of the Bloch–Redfield model, upon varying the qubit frequency, the state vector rotates around the z-axis. Thus, upon the change $\delta\omega_{10}$, the corresponding rotation will occur by the angle $\varphi = 2\pi\int\delta\omega_{01}(t)\,\mathrm{d}t$ provided that the operation is executed adiabatically and does not change the level populations. Usually, to realize such changes, trapezoidal flux pulses with a duration of a few nanoseconds long are used through a separate control line.

Such an approach allows getting an advantage in time and precision of operations, since the above virtual gates require using several operations for one rotation around the z-axis, and the accuracy of Z-rotation depends on the accuracy of all operations used for this aim.

3.5 Basic problems in implementing single-qubit operations and their solutions

Using a flux line allows using Z-gates simultaneously with X- and Y-gates. However, at the same time, an unwanted interaction of the flux line with qubits appears. This effect could be reduced using the bilayer technology for processor fabrication (Fig. 8) similar to the flip-chip method. Qubits are located in one chip, whereas the control and readout elements are in another. The chips are connected capacitively with each other using the bump-bonding technology. Using additional lines of flux control requires careful analysis of the nuances of their 'coexistence' with quantum registers. There is a method for extracting exact parameters of the line (S-, Y-, and Z-matrices), where the qubit itself is used as an analyzer [49].

As was discussed in Section 2.1, when executing quantum operations, the presence of higher energy levels in the qubit system must be taken into account. These levels can give rise to two types of errors: a loss of information because of 'leakage' of the population of the other, higher energy levels, not belonging to the computational space, and phase disturbance due to the coupling between the computational

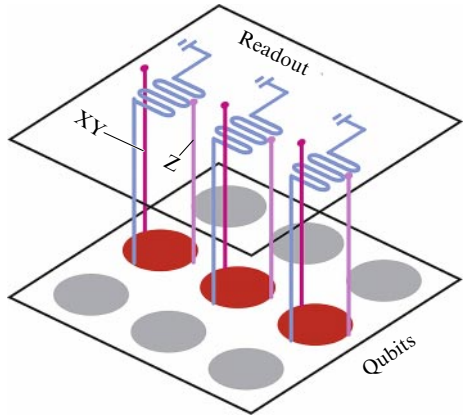

Figure 8. (Color online.) Arrangement of qubits and control elements in a flip-chip circuit.

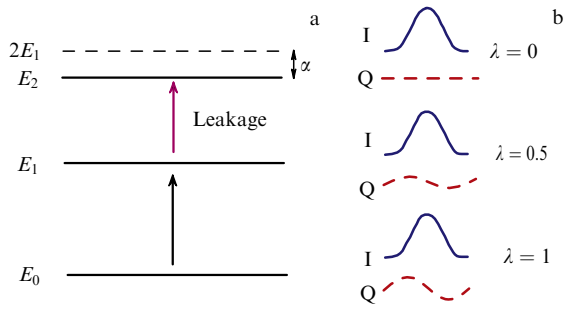

Figure 9. DRAG circuit. (a) Channel of leakage to higher states of the qubit. (b) Pulse shapes for various smoothing parameters.

space levels and the higher ones, which is manifested when an external electromagnetic field is applied to the system. Because of the transmon weak anharmonicity, the effect of the above factors appears to be rather strong. To solve the 'leakage' problem, derivative removal via an adiabatic gate (DRAG) control system was developed that reduces the probability of such errors. This scheme is a protocol of correcting the shape of single-qubit gate pulses of the form

$$V_{\mathrm{d}}(t) = V_0 f(t)\,, \quad f(t) = \begin{cases} f(t) \to f(t) & \text{in I channel,} \\ f(t) \to \dfrac{\lambda}{\omega_\alpha} f'(t) & \text{in Q channel,} \end{cases} \tag{16}$$

where λ is the smoothing parameter. Studies have shown that the optimal value of λ lies in the range from 0.5 to 1 [50–53]. There is a similar protocol for the above-mentioned virtual Z-gates, which are a combination of X- and Y-gates. Such a protocol, called DRAGZ, allows reducing the rate of phase errors [54] (Fig. 9).

According to the literature data [17, 55], there is a certain threshold value of nonlinearity, starting from which the dynamics of two lower energy levels is well isolated ($E_C \ll E_{\mathrm{J}}$). As shown in Ref. [17], in the Duffing–Hubbard approximation, this leads to a limitation affecting the duration of control Rabi pulses, $\tau_p = 1/|\omega_{01}\alpha_{\mathrm{r}}|$, where $\alpha_{\mathrm{r}} = -(8E_{\mathrm{J}}/E_C)^{1/2}$. Thus, the implementation of X- and Y-gates is limited in time, consequently limiting the overall speed of operations in quantum registers.

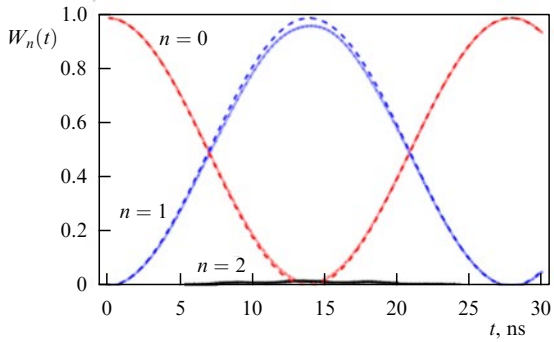

Figure 10. (Color online.) Dynamics of nonlinear oscillator level populations W_n ($n = 0, 1, 2$) (4). Solid curves show results of numerical simulation, dashed lines correspond to theoretical dependence (12). Parameters of the system and the action are characteristic of the transmon [17]: $\omega_{01}/(2\pi) = 5$ GHz, $\omega_{12}/(2\pi) = 4.8$ GHz, $E_C/h = 0.25$ GHz, $E_{\mathrm{J}} = 50E_C$, $\delta\omega/(2\pi) = 1$ MHz, $A_\Omega = 0.23$ GHz.

Therefore, it is an important issue to find an optimal regime of qubit functioning with the minimum 'leakage' (less than 1%) to the higher-lying energy levels. The leakage can be defined as the relative probability of populating the higher levels W_n in a nonlinear oscillator (4) in comparison with the populations of two lower energy levels (basis states $|0\rangle$ and $|1\rangle$ of the qubit). We performed a numerical analysis of the dynamics of the nonlinear multilevel quantum system (4) with parameters characteristic of a transmon. The results of the analysis are presented in Fig. 10. It is seen that the Rabi oscillations of the populations of the nonlinear oscillator (4) states correspond to the two-level approximation, when it is possible to consider the two basis states $|0\rangle$ and $|1\rangle$ with energies $E_0 = 0$ and $E_1 = \hbar\omega_{01}$ of the real system. The population of the second excited state $|2\rangle$ does not exceed 1%, and the populations of all other higher energy levels ($n > 2$) are negligibly small, $W_n \ll W_2$. The minimal time to invert the states at typical parameters is ≈ 14 ns, which by order of magnitude coincides with the data obtained based on the Duffing–Hubbard effective Hamiltonian [55].

3.6 Two-qubit operations

The use of two-qubit gates gives rise to a number of new difficulties. In contrast to the single-qubit operations that require isolation of a qubit from other parts of the quantum processor, including the neighboring qubits, two-qubit operations require a connection between the individual artificial atoms. There are many types of two-qubit operations, from which it is possible to distinguish the two most widespread classes. First, this is the SWAP operation and its modifications related to the exchange of states between qubits, in particular, iSWAP. Second, these are 'operations with control,' in which the execution of an operation in one qubit occurs depending on the state of the other qubit. Such operations include, for example, CNOT and CZ. Two-qubit gates are more sensitive to noises than the single-qubit ones. This is associated not only with the summation of noises from individual qubits but also with the presence of noises in the chosen method of connection (e.g., the use of a resonator introduces a photon noise). To determine the efficient regime of operation for two-qubit gates, special protocols of measuring parasitic effects [56] and optimization [57–59] are used.

Among the two-qubit gates, it is possible to conventionally separate a group, implying the possibility of resonator tuning, including, e.g., the Direct Resonance iSWAP (DRi) [60], Dynamical CPhase (DP) [61], or the use of tunable connections. Another type of gate uses transmons with a fixed frequency, such as Resonator Sideband Induced iSWAP (RSi) [62], Cross Resonance gate (CR) [63, 64], Bell–Rabi gate (BR) [65], Resonator Induced CPhase (RIP) [66], Microwave Activated CPhase (MAP) [67], or Blue-sideband SWAP (bSWAP) [65]. Both approaches have their advantages and disadvantages. For example, the use of tunable qubits allows better isolation of qubits for performing single-qubit operations, since there is a possibility to detune qubits from each other. The cost of this possibility is a reduction in the coherence time because of the increased sensitivity of tunable qubits to flux noise. This approach requires additional control lines, which increases the complexity and general noisiness of the system. In turn, using qubits with a fixed energy spectrum allows achieving longer lifetimes, because they can be fabricated already tuned to the regime of minimal sensitivity to flux noise. The main drawback of such an approach is the impossibility of controlling the qubit parameters, which makes it necessary to have a tunable connection or special protocols not using qubit tuning operations. Let us consider some protocols characteristic of both tunable and nontunable qubits.

3.7 Implementation of iSWAP, CZ, and ZZ gates

The iSWAP gate swaps the states of two qubits, imparting to them an additional phase of $\pi/2$, which can be implemented for tunable qubits [68]. For this purpose, one qubit is prepared in the excited state and the other one in the ground state. Then, the frequency of both elements of the processor is tuned close to the point of avoided crossing of their energy levels and a flux pulse Φ_{SWAP} is supplied to the two-qubit system, which shifts the qubit energy values and increases interaction between the qubits (Fig. 11). An additional phase incursion arises when the qubit approaches the avoided crossing, the bypass contour chosen to make the additional phase exactly equal to π.

There is also a way to implement this gate without flux control. This method is suitable for nontunable qubits and is executed following the cross resonance (CR) protocol [63, 64]. The main idea behind this method is similar to the microwave one described above — the creation of a short-lived resonance with alternating current pulse instead of a magnetic flux. The interaction occurs due to the Stark effect.

However, not all the gates can be conveniently implemented within the subspace of states $|0\rangle \otimes |1\rangle$. There are a number of operations using the higher-lying energy levels of the qubit, particularly efficient in transmons due to their weak anharmonicity.

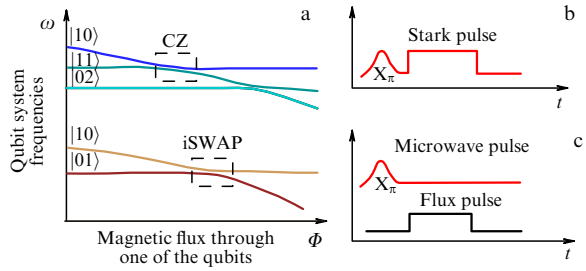

Figure 11. (Color online.) Implementation of iSWAP and CZ gates. (a) Energy diagram for iSWAP gates (in the computation subspace $|0\rangle \otimes |1\rangle$) and CZ (beyond the computational subspace). (b) Shape of the current control pulses for the CZ gate implementation. (c) Shape of the current control pulses for the iSWAP gate implementation.

The gate CZ [69, 70] belongs to the latter. It changes the state of one qubit of a pair (rotates its phase by π) only when both are in the excited state. In order to change the phase, the system approaches the avoided crossing $|11\rangle - |02\rangle$ adiabatically (see Fig. 11). The adiabaticity is necessary to avoid leakage to the second excited level. By means of additional control techniques, the CZ gate efficiency could been brought to 99.999% [71].

There are also a number of protocols with control by microwave pulses only. Consider, for example, the microwave activated phase (MAP) protocol [67] using more than three energy levels of a qubit (Fig. 12a). Such a solution is used in systems where the state $|12\rangle$ is located nearly at the same level as $|03\rangle$, but there is no degeneracy of any other energy levels. By analogy with the Stark effect, a short microwave pulse shifts levels $|12\rangle$ and $|03\rangle$ towards each other, and an interaction occurs between them. Because of the difference between the energies of transitions $|12\rangle \leftrightarrow |03\rangle$ and $|11\rangle \leftrightarrow |02\rangle$ during sequential transitions of transmons to their highly excited states, an additional phase incursion arises, which leads to the implementation of the Ising gate

$$ZZ_{\pi} = \begin{vmatrix} \mathrm{i} & 0 & 0 & 0 \\ 0 & -\mathrm{i} & 0 & 0 \\ 0 & 0 & -\mathrm{i} & 0 \\ 0 & 0 & 0 & \mathrm{i} \end{vmatrix}.$$

At a relatively large duration (0.5 μs), such a gate requires only microwave control, and it has performed well in processors based on nontunable qubits with fixed connections.

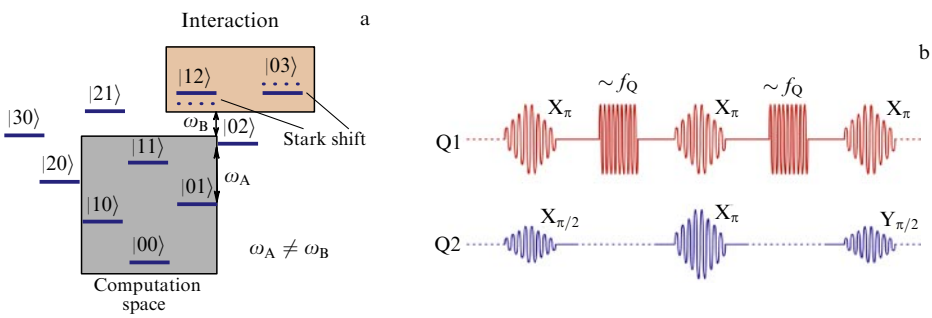

Figure 12. (Color online.) Implementation of the MAP gate. (a) Diagram of energy levels used to implement the MAP gate. (b) Shape of the pulses supplied to qubits.

The basic principles of the modern implementation of control gates include the use of quadrature mixers, the 'smoothing' of the pulses to control the transitions to a higher energy states, and the extension of the computational space to higher levels if necessary. In particular, based on these principles, protocols were developed that allow implementing CPhase gates with a duration of less than 100 ns [72], adiabatic holonomic gates less sensitive to noise [73–76], adiabatic two-qubit gates with a duration of only 19 ns [77], easily calibrated two-qubit XY-gates [78], CZ gates based on bipolar flux pulses [79], and methods of gate acceleration using parametric modulation [80].

3.8 Architecture and implementation of interqubit connections

High-quality single-qubit operations require the absence of interaction with neighboring qubits, whereas for multi-qubit operations its presence is necessary. Let us consider the main problems that arise when choosing a method of physical connection between the qubits. Today, it is possible to select several solutions for the physical implementation of interqubit connections: to connect qubits directly via a capacitance, a resonator, or an additional Josephson junction. Let us dwell on the particular kinds of connections in more detail.

3.8.1 Direct capacitive connection. The direct capacitive connection is very simple to implement physically. It is sufficient simply to place two qubits close to each other or add an element providing an effective capacitance between them (Fig. 13a). Such a connection is also rather compact, since no additional elements are needed or they can be easily included in the architecture design. The effective Hamiltonian of such a connection can be written as

$$H = \hbar g_{12}(\sigma_1^+\sigma_2^- + \sigma_2^+\sigma_1^-)\,, \tag{17}$$

where $\sigma^+ = |1\rangle\langle 0|$, $\sigma^- = |0\rangle\langle 1|$, and $\hbar g_{12} = 4e^2 C_{12}/(C_1 C_2)$ is the connectivity strength.

This connection is constant and its strength depends only on the detuning between the excitation frequencies of the qubits (the maximum strength of connection being naturally observed in resonance). For this reason, capacitive connections have proven themselves well in systems of tunable qubits (particularly in Rigetti processors, to be discussed in Section 3.9).

3.8.2 Resonator connection. An advanced version of the capacitive connection is the connection via an additional resonator between two qubits [81]. The main difference in the resonator connection from the direct capacitive one is that the presence of a resonator adds new degrees of freedom to the system. The qubits are now connected not directly but through an additional multilevel system (Fig. 13b); therefore, instead of one frequency detuning between two qubits, it is necessary to consider two frequency detunings of individual qubits from the resonator. The effective Hamiltonian of the connection takes the form

$$H = \hbar\frac{g_1 g_2}{2\Delta_1\Delta_2}(\Delta_1 + \Delta_2)(\sigma_1^+\sigma_2^- + \sigma_2^+\sigma_1^-)\,. \tag{18}$$

We assume that $\Delta_1 \gg g_1$, $\Delta_2 \gg g_2$, where $\Delta_{1,2} = \omega_{01}^{1,2} - \omega_r$ are the detunings of the qubit frequencies $\omega_{01}^{1,2}$ from the resonator frequency ω_r. Therefore, by controlling the detuning of each of the qubits, it is possible to tune their connection strength. A disadvantage of such an approach compared to the direct capacitive connection is the necessity to create a resonator with the specified parameters, which may not be simple within the limited space of the chip.

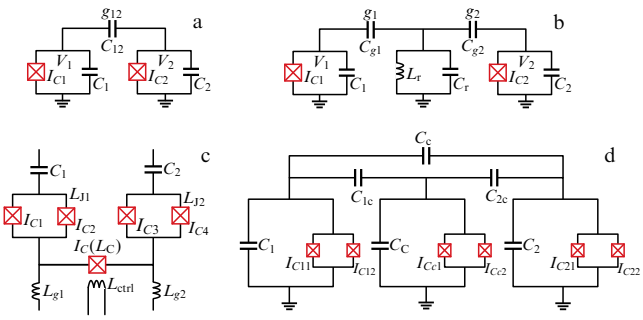

Figure 13. Interqubit connection circuits. Parameters of the elements are indicated in the figure. Circuits implement a (a) capacitive interqubit connection, (b) resonant interqubit connection, (c) Josephson interqubit connection, (d) modified Josephson interqubit connection with additional shunting.

3.8.3 Josephson connection. There are also interqubit connections with a tunable strength. The first technical solution for a tunable connection was the gmon scheme [82] developed by Google. The gmon is a modification of the Xmon discussed in Section 2.3.4, with additional inductances controlling the current strength flowing from qubit to qubit and, therefore, the strength of the connection between them. Gmons are connected inductively (Fig. 13c), which allows a considerable reduction in the energy accumulated in the system of interqubit connections. Therefore, the related losses are reduced as well and, correspondingly, the decoherence time increases. Moreover, this allows getting rid of the connection mechanisms based on direct current and hence reduce the cross noises caused by the interaction of circuit elements. The possibility of tuning removes the problem of frequency oversaturation, when the processes inside the system occur at close frequencies, giving rise to parasitic resonances. The adiabatic tuning of the connection allowed performing gate operations for several qubits at speeds comparable to those of single-qubit operations.

The interaction Hamiltonian can be expressed in terms of the mutual inductance M and the coupling inductances L_g and L_J (we assume that in the circuit $L_{g1} = L_{g2} = L_g$ and $L_{J1} = L_{J2} = L_J$):

$$H = -\frac{\omega_{01}}{2}\frac{M}{L_g + L_J}(\sigma_1^+\sigma_2^- + \sigma_2^+\sigma_1^-)\,. \tag{19}$$

Due to this, the connection strength is expressed in terms of inductances,

$$g = -\frac{\omega_{01}}{2}\frac{L_g}{L_g + L_J}\frac{L_g}{2L_g + L_C}\,, \tag{20}$$

where $L_C = \Phi_0/(2\pi I_0 \cos\varphi_c)$, and φ_c is the phase difference at the connecting Josephson junction.

The decoherence time change due to the presence of tunable connection in gmons may be an issue. Indeed, the inductances L_g and L_J in the system may become an additional source of flux noise. The problem is solved by operating the interqubit connection at low voltages, which reduces the noises at the connecting Josephson junction by $(L_J/L_g)^2$ times. An important application of such a connection method is the potential to isolate individual qubits to

perform local operations, in essence, 'switching off' individual connections between neighbors, made possible, inasmuch as the connection strength can be varied from negative to positive values, passing through zero at $\varphi = \pi/2$. Reference [83] demonstrates an operation mode in a system of several qubits in the absence of a connection ($g = 0$). However, the lifetime of gmons (5–10 μs) is less than that of a nontunable Xmon (20–40 μs), so that a problem arises as to how to reduce the tunable connection effect on the qubit operation. To suppress noises [84], a Josephson junction shunting scheme by capacitances C_{1c}, C_{2c}, and C_c of the same order of magnitude, exceeding the transmons' own capacitance, was developed (Fig. 13d). In fact, the inductances in the gmon scheme are replaced with capacitances, which allows reducing the characteristic size of the connection and simplifying processor fabrication:

$$g_{12} \approx \frac{1}{2}\left[\frac{C_{12}}{\sqrt{C_1 C_2}} + \frac{C_{1c}C_{2c}}{\sqrt{C_1 C_2 C_c^2}}\right]\sqrt{\omega_1\omega_2}\,. \qquad (21)$$

This rather simple circuit allows completely switching off the interqubit connection and suppressing the errors arising in gate operations. As a consequence, the lifetimes here approach 20–40 μs, i.e., the times demonstrated by Xmons without a tunable connection. Noises caused by the additional connection practically appeared to be completely leveled.

It is possible to formulate criteria for choosing the architecture of a quantum processor as follows: (1) the qubit frequency tuning possibility; (2) the qubit connection strength tuning possibility. As is seen from the considered types of connections, the tunability of the qubits themselves, as well as the connections between them, simplifies the control, but increases the system noisiness (thus reducing the relaxation and dephasing time) because of more noise sources introduced by the addition of control lines.

3.9 Review of existing quantum processors

Now let us compare the particular processors created by the leading research teams by their basic characteristics (Table 1) and characteristic time of executing operations (Table 2).

The IBM processors are based on nontunable transmons (see Section 2.3.3) with large decoherence time connected by resonators. It is impossible to switch off the connection between the qubits. The 16-qubit Rueschlikon (Fig. 14a, b) with the ladder architecture [85–91] is an example of such a processor. The company has also developed three 20-qubit processors, Tokyo, Poughkeepsie, and Boeblingen [92–94]. The topology and the connection type are the same as in Rueschlikon, but all three processors have a rather nonstandard architecture.

The Rigetti Company uses concentric transmons with reduced sensitivity to flux noise as basic elements of their quantum computers (see Section 2.3.2). Papers [95–100] describe computations using the Rigetti 8Q Agave processor (Fig. 14c, d) with a linear architecture of eight qubits, closed in a ring. The interqubit connections are capacitive, and, as such, the qubits are separated by a considerable distance, the mutual capacitance being created by an additional capacitor. Fixed-frequency qubits alternate with tunable ones, which allows detuning the processor elements and 'switching off' the interaction between them, although not all of the qubits are tunable. Such an alternation of qubits of two types allows reducing the number of 'noisy' control lines in the processor. The Rigetti 19Q processor with 20 operating qubits is based on the same architecture [101–105].

One of the last Google developments is the Sycamore processor (Fig. 14e, f), consisting of 53 tunable Xmons (see Section 2.3.4) [7, 106, 107]. The processor architecture is a rectangular lattice of 6×9 qubits (initially 54 qubits were created, but one of them did not work), which is optimal for testing surface codes for quantum error correction. Control and readout lines are located on the processor substrate. When designing the Sycamore, the stress was on creating a strong enough connection between the processor elements to accelerate two-qubit operations with relatively few errors. The connections were not fixed: using Josephson connections, the possibility of tuning was provided to 'switch off' qubits, thus reducing their influence on neighbors.

At present, rather complex procedures for quantum processor calibration are being developed to reduce the

Table 1. Comparative table of parameters of up-to-date quantum superconducting processors.

Processor	Number of qubits	Connection type	Qubit lifetime, μs	Average operation time, ns	Average circuit depth
IBM Q16 Rueschlikon	16	Resonant	28	210	130
IBM Q20 Tokyo	20	Resonant	34	330	105
Rigetti 8Q Agave	8	Capacitive	15	155	95
Rigetti 19Q Acorn	19	Capacitive	10	180	55
Google Sycamore	53	Josephson	15	25	600

Table 2. Comparative table of fidelity parameters of executing operations with the most up-to-date quantum superconducting processors.

Processor	Fidelity (1Q-gate)	Fidelity (2Q-gate)	Fidelity (readout)
IBM Q16 Rueschlikon	99.735	No data	97.13
IBM Q20 Tokyo	98.01	97.16	93.21
Rigetti 8Q Agave	98	98	92
Rigetti 19Q Acorn	98.5	87	90
Google Sycamore	99.84	99.4	96.2

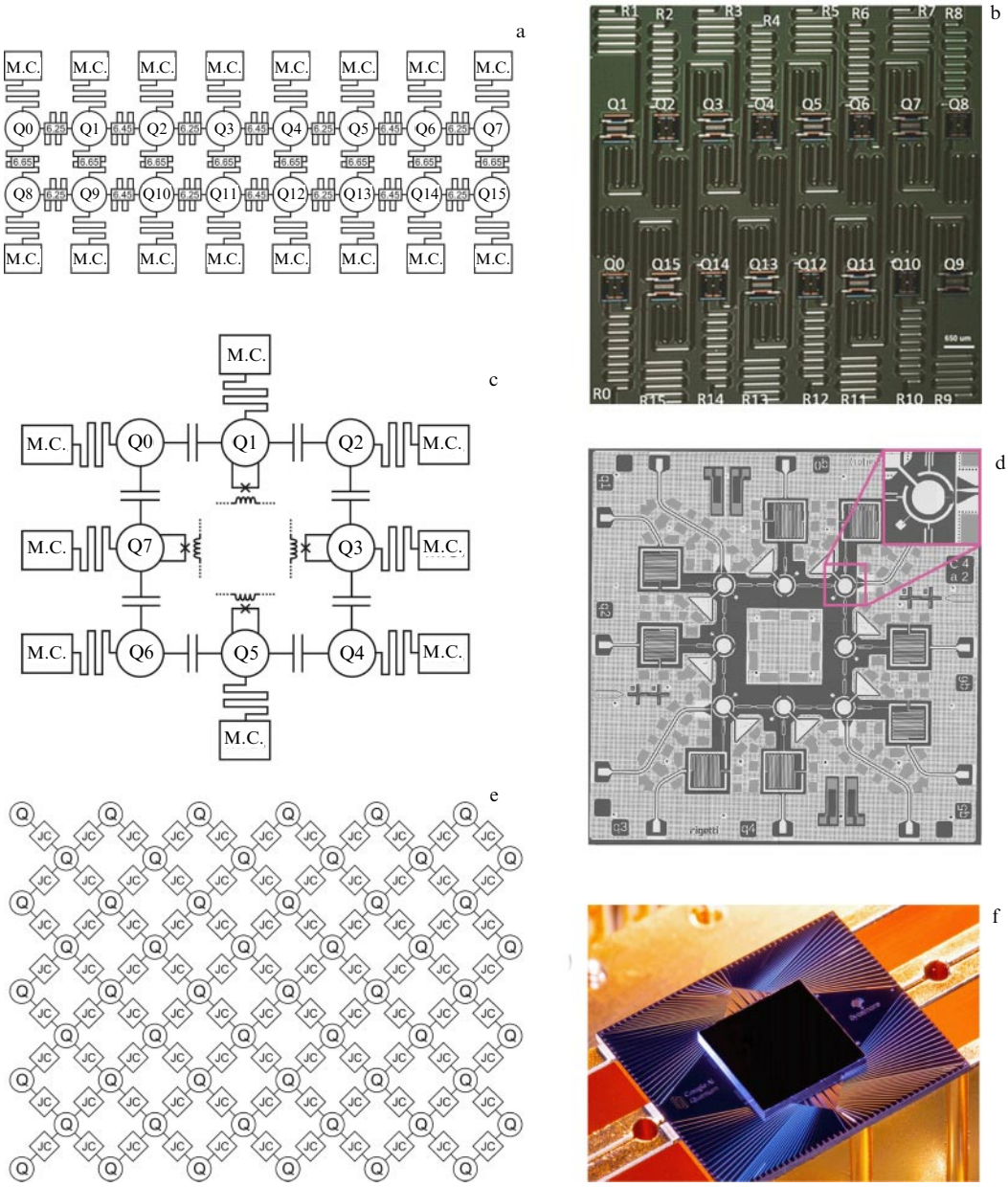

Figure 14. (Color online.) Circuits of existing quantum processors. Notation: Q_i — qubit number i, M.C. — microwave control element, JC — Josephson connection. (a) Equivalent circuit of IBM Q16 Rueschlikon processor; numbers on resonators indicate their frequencies. (b) Chip microphotograph of the IBMQ16 Rueschlikon processor; readout resonators are marked as Ri. (c) Equivalent circuit of Rigetti 8Q Agave processor. (d) Chip microphotograph of the Rigetti 8Q Agave processor. (e) Equivalent circuit of Google Sycamore processor. (f) Chip microphotograph of the Google Sycamore processor.

errors of individual gates and to perform a readout. The Sycamore processor, which was exactly the one to demonstrate quantum supremacy in 2019, is a vivid example of both the significance and the complexity of such an operation. The Sycamore calibration process allows to reduce qubit errors of all types by determining the set of control parameters. Each qubit requires about a hundred of such control parameters. The calibration process is visualized by a complex directed graph, each node of which corresponds to optimizing one group or another of parameters responsible for particular quantum operations. The calibration of the Sycamore processor takes about 36 h. A special optimizer called Snake was specially developed and patented for this task [7].

4. New concepts in controlling multi-particle quantum systems

4.1 Analog-digital approach to implementing logical operations

The approach to quantum computing using Rabi pulses described in Section 3.3 suffers from a known drawback — the accumulation of errors of individual quantum operations in the process of algorithm execution. To implement algorithms of practical significance, it is required to use a large number of quantum operations, the more qubits are involved in the algorithm, the bigger the number of operation grows. Hence, a necessity arises to develop alternative methods of

performing quantum computations, partially bypassing the problem of error accumulation. One such method is analog-digital.

The main idea behind this method is to use the physical interaction of qubits in the system instead of representing the required state transformation through the standard set of gates. In this approach, the register of qubits is controlled by single-qubit operations and the evolution caused by the interaction of physical qubits that ensure quantum entanglement. The interaction Hamiltonian is 'built into' the multi-qubit circuit at the physical level due to the connections between the qubits. This allows avoiding the use of two-qubit operations, whose execution errors in real processors are currently too large.

According to theoretical models, the approach described above allows implementing an arbitrary unitary transformation [108], in particular, the quantum Fourier transform [109]. This quantum simulation approach is implemented with superconducting qubits [110], as well as ion-trap-based systems [111, 112]. The initial state of the qubit register was prepared using single-qubit gates, after which the system evolved because of the physical interaction between the qubits. As a result, it was possible to observe signs of multiparticle localization in such artificial spin systems.

An example of analog-digital simulation using the residual interaction between the qubits of an IBM processor was demonstrated in recent paper [113]. In contrast to [110–112], the authors of [113] use the Trotter–Suzuki expansion of the system evolution operator, in which the application of entangling operations is periodically alternated with the use of single-qubit rotations. The qubit entanglement is implemented through interaction, and that imposes some limitations on the character of interactions and connection topology of the simulated system. However, the involvement of single-qubit operations imparts a certain flexibility to the technique. First, by using them, it is easy to simulate stochastic processes, expressed by the single-particle terms of the Hamiltonian. Second, using single-qubit gates, one can change the basis, which makes it possible to proceed effectively in the evolution operator from an XX-type interaction to YY and ZZ types, as well as to their arbitrary combinations. Third, the change in the interqubit connection can be implemented using the spin echo technique.

As an illustration, the authors of [113] implemented an algorithm that simulates the dynamics of clusters, containing up to 16 spins, described by the Ising model in a transverse field. The results were compared with those of quantum computations using the same processors, in which standard CNOT gates were used instead of entangling operations at the expense of residual interaction. Also, the quantum Fourier transform has been modeled using three qubits. This example demonstrated the superiority of the analog-digital method in the accuracy of simulation over the usual digital approaches.

The above results show that it is relevant today to create specialized quantum processors aimed at implementing particular quantum algorithms based on the analog-digital strategy. It is worth paying special attention to the search for ways to reduce the duration of all key logical operations.

4.2 Superconducting numerical schemes for controlling qubit states: a general concept

The large number of microwave channels necessary to control multi-qubit systems is also a serious problem. Each of these channels requires rather expensive equipment (sources of coherent microwave radiation with a fixed carrier frequency and specified pulse duration, high-stability signal generators, quadrature mixers, and amplifiers), as well as a multitude of coaxial lines and elements for generating and transmitting signals into a low-temperature medium.

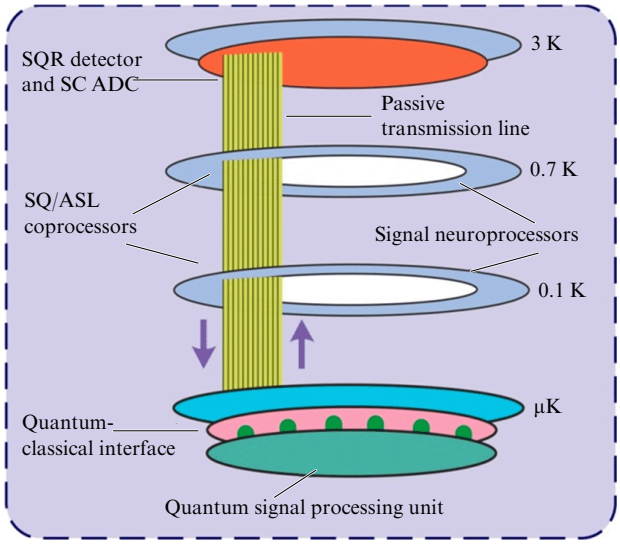

Figure 15. (Color online.) Schematic of using classical and quantum coprocessors within a unique cryogenic complex. System also comprises an array of quantum registers with control, readout, and error correction circuits. Connections among the superconducting classical and quantum coprocessors, data processing quantum unit, and high-temperature environment are implemented through transmission lines with amplifiers/converters at all intermediate stages [114]. SQR detector — superconducting quantum radio wave detector, SC ADC — superconducting analog-to-digital converter, FSQ/ASL — fast single-quantum/adiabatic superconducting logic.

Each control channel plays the role of a channel of heat transfer from the environment to the quantum computing system, reducing the decoherence time for all qubits of the processor. Consequently, the control of processors comprising a few hundred qubits or more will require fundamentally new approaches.

To solve this problem, it was proposed to use 'classical' superconducting processors based on niobium technology, whose operating temperatures are from 3 to 4 K. The interface circuits that connect different units of the computing system, important for its operation, can be implemented based on Josephson transmission lines (JTLs) with extremely low dissipation (proposed earlier for the readout of quantum bit states). An analysis of the effect of soliton-like excitations (fluxons) propagating through such nonlinear Josephson lines on the dynamics of the quantum system states proved the practicability of controlling qubit states by applying voltage or magnetic flux pulses. A radical reduction in extremely unwanted energy dissipation in the process of such manipulations (of the order of 1 aJ) is possible upon a transition to adiabatic (reversible) transmission lines (ATLs). The application of flip-chip technology, as shown in Fig. 15, can allow one to use efficiently the cryostat space to reduce additional heat flows through the control channels and to improve the quality of quantum processor control and the processing of operation results.

Initially, superconducting digital devices were developed for fast and energy-efficient classical computing complexes

[115]. In the rapid single flux quantum (RSFQ) logic used in such systems, the classical bits are encoded by the presence or absence of a magnetic flux quantum (and related vortex current) in a superconducting contour. A superconducting contour with a pair of Josephson junctions plays the role of an elementary cell, analogous to a transistor in semiconductor electronics. The method of transmitting information in the form of integer quanta of magnetic flux from cell to cell is based on the use of JTLs, which are circuits of Josephson junctions connected in parallel by inductive elements. The JTL goes into the operating regime when a current of a certain strength is supplied to each of the Josephson junctions. The pulse of current that comes from a logical cell will switch the first of the JTL junctions to a resistive state, causing a redistribution of currents, and a vortex current will arise in the circuit (related to a quantum of magnetic flux), which will start propagating along the transmission line. It can be said that an excitation (fluxon) is transferred from cell to cell in the chain of superconducting contours with Josephson junctions. The wave of currents and voltages related to this propagating quasi-soliton excitation can be used to control the qubit state or to read it out.

Recently attempts have been made to adapt the versions of digital superconducting control circuits to a quantum processor. To act on individual qubits, nanosecond sequences of solitary nonmodulated pulses of picosecond duration (fluxon excitations in the Josephson medium) were used. It was shown that, to create such sequences with a controlled pulse repetition rate (an analog of the control pulse carrier frequency in the Rabi technique described in Section 3.3), schemes of superconducting RSFQ logic can be used [116–118].

An important problem with digital control is choosing a scheme to specify control single flux quantum (SFQ) pulses, which can be generated by a device known as a DC/SFQ converter [119]. This device converts an analog radiofrequency signal into a set of SFQ pulses, additionally using a DC power supply (Fig. 16). Upon exceeding a certain current strength determined by the critical currents of Josephson junctions of the converter, the generation of pulses begins. Thanks to the relative simplicity of implementation and low number of Josephson junctions, such a model of a DC/SFQ converter is perfectly suitable as an element of qubit control. The converter circuit can be additionally optimized by power [120–124]. The generator of SFQ pulses is connected to a qubit via a coupling capacitance. However, using this type of converter may lead to additional quasiparticle poisoning of qubits.

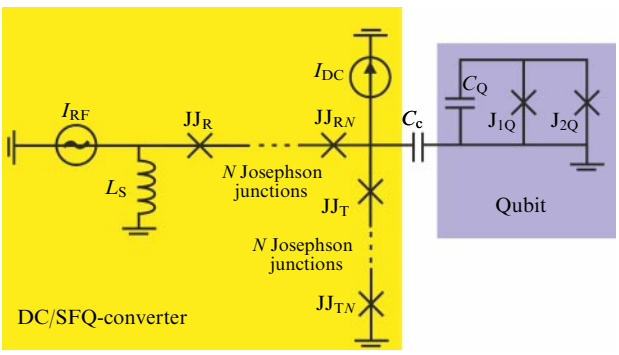

Figure 16. Circuit connecting a DC/SFQ converter on single contacts to a transmon.

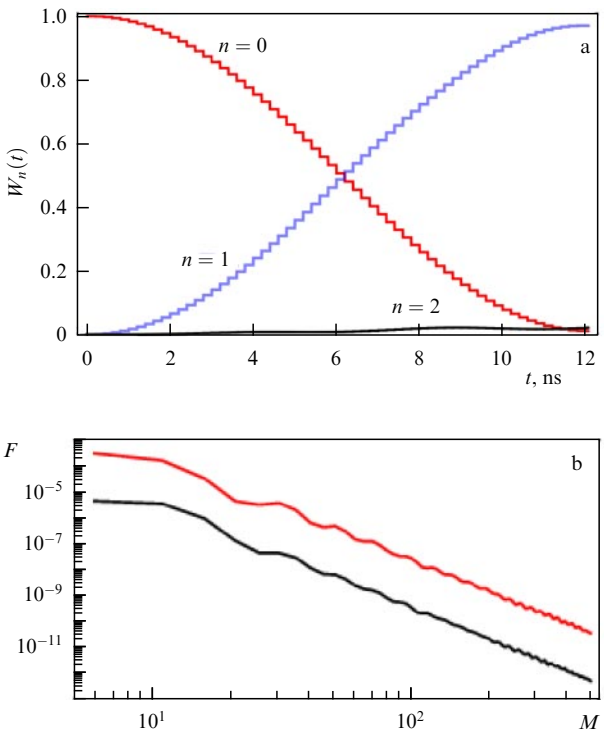

Figure 17. (Color online.) (a) Dynamics of transmon level populations (4) W_n $(n = 0, 1, 2)$ under the action of a sequence of $M = 60$ unipolar pulses with parameters $A = 1$ GHz, $\tau = 4$ ps, $\tau_d = 200$ ps. (b) Error probability for the operations of rotating the Bloch vector by π (red curve) and $\pi/2$ (black curve) because of state leakage from the computation basis depending on the number of SFQ pulses in the regular control sequence. Qubit parameters are given in Fig. 10.

In this area, noticeable success was recently achieved: it appeared possible to implement qubit control using sequences of picosecond unipolar pulses [125–128].

4.3 Implementation of single-qubit operations using short unipolar pulses

Qubit control, both using short unipolar pulses and within the Rabi technique, allows implementing a complete set of one- and two-qubit operations. To begin, let us consider how to realize a single-qubit gate by means of M short unipolar pulses. Figure 17 demonstrates an implementation of a quantum single-qubit NOT operation using a sequence of $M = 60$ pulses with a duration of $\tau = 4$ ps each. The interval between pulses was $\tau_d = 2\pi/\omega_{01} = 200$ ps. A numerical analysis of population dynamics (Fig. 17a) is carried out taking into account the transmon higher-lying energy levels (as was done in Ref. [125]); control unipolar action $\varepsilon(t)$ is presented in the form

$$\varepsilon(t) = \sum_{j=1}^{M} A\Theta\left(t - \left(j\tau_d - \frac{\tau}{2}\right)\right)\Theta\left(\left(j\tau_d + \frac{\tau}{2}\right) - t\right), \quad (22)$$

where A is the unipolar pulse amplitude, and $\Theta(t)$ is the Heaviside function.

From Fig. 17, it is seen that the probability of 'leakage' to higher energy levels does not exceed 1% for the calculation parameters chosen, and each of the pulses in the sequence causes a cascade of rotations on the Bloch sphere. Upon increasing the number of pulses, the 'leakage' to higher levels decreases as $\sim M^{-2}$ [125] (Fig. 17b). The interval between the

pulses corresponds to an integer, a multiple of the period of oscillations at the qubit frequency, due to which the state vector executes a coherent rotation on the Bloch sphere during the intervals between the pulses. Such a sequence of pulses was called DANTE (Delays Alternating with Nutations for Tailored Excitation) [129, 130]. The total duration of operations performed using long sequences of 'single-quantum' pulses of the field (fluxons) exceeds 10 ns. The use of complex sequences of single-quantum pulses with a variable off-duty factor allows getting an operation accuracy above 99.99%, comparable with that of the best operations performed using the microwave technique, sufficient to implement error correction algorithms [126].

Using fast single-quantum logic to control qubits can reduce their decoherence time due to the above-mentioned quasiparticle poisoning when placing quantum and classical logical circuits on one chip. In this case, the accuracy of operations using long sequences of single-quantum pulses in practice appears to be lower than using shorter ones [128]. This is explained by the fact that the total number of generated quasiparticles (affecting the qubit either directly through the diffusion channel or via the phonons produced) depends on the number of switchings of the Josephson junctions in the logical circuits [131].

Experimental studies of the quasiparticle poisoning in this case showed that, for short sequences (100 pulses or fewer), the number of the formed nonequilibrium quasiparticles near the logical gates turns out to be too small for substantial phonon action on the qubit, since the processes of recombination and phonon emission require a high local density of quasiparticles. For longer sequences, the number of quasiparticles acting on a qubit linearly grows with an increase in the switching number of Josephson junctions, so that one switching corresponds to approximately 2×10^{-3} quasiparticles. When a delay is introduced between the quasiparticle poisoning and the measurement of the qubit relaxation time, an exponential decrease in the effective number of acting quasiparticles was observed, with the effective capture time being of the order of 17 μs.

If the digital circuits used for control and quantum circuits are located on different chips integrated in a single multichip module, then the single-quantum pulses arrive at a quantum chip through a capacitive connection. Choosing iridium contact sites can provide a low-energy barrier to quasiparticle diffusion between the chips. In this case, the recombination phonons, produced by quasiparticles in the indium contacts, will have insufficient energy for breaking Cooper pairs in the niobium layer on the quantum chip.

Decreasing the critical current of Josephson junctions in logical circuits can increase the decoherence time, since the energy released in the process of junction switching is proportional to the product of the critical current and the magnetic flux quantum. The operating temperatures are a few tens of millikelvins, so that the critical current value may differ from that typical of circuits operating at the liquid helium temperature (4.2 K) by two orders of magnitude without increasing the false triggering rate caused by thermal fluctuations. However, the reduction in the critical current will give rise to the necessity to increase the inductance of the circuits, which will result in increasing their size.

Significant suppression of quasiparticle poisoning can be achieved using the metallic traps mentioned above. Having diffused to a normal metal, a quasiparticle interacts with electrons and quickly relaxes in energy below the gap threshold, which makes impossible its return to the superconductor.

Ultimately, new methods of implementing RSFQ circuits for the superconducting qubit state fast control are currently being developed using a small number of unipolar pulses [132–138]. It is worth noting that in this case the maximum acceleration of operations can be achieved by using flux qubits rather than transmons. The decoherence time in flux qubits can be noticeably higher, and the transition frequencies, on the contrary, lower than in transmons, so that operations within the traditional Rabi technique take more time. At the same time, the large anharmonicity in flux qubits, $\omega_{12} \gg \omega_{01}$, allows increasing the amplitude without increasing the 'leakage' and implementing gates with a small number of ultrashort pulses. As a result, the operation time becomes noticeably shorter than in transmons.

This technique of control in a superconducting two-qubit register allows a substantial acceleration of executing quantum algorithms [139–142].

Let a qubit be affected by a single rectangular pulse of the form (22) only. The characteristic time of fluxon action on the qubit depends on the plasma frequency, which in turn is proportional to the square root of the critical current in Josephson junctions. If we take, for example, widespread technological processes with the current densities of 20 kA cm^{-2} and 30 A cm^{-2} (the first is used in fast digital circuits, the second, in low-temperature electronics, in particular, in parametric amplifiers), then, for the plasma frequency, we can obtain values at the level of 465 and 25 GHz, respectively. This means that the characteristic duration of one control pulse can be reduced to the subnanosecond level.

The probability of a 'flip' of the qubit state $|0\rangle \leftrightarrow |1\rangle$ under the action of one unipolar pulse is determined in the two-level approximation by the Rabi formula (12):

$$W_{01} = 1 - W_0(t) = \frac{A_\Omega^2}{\Omega^2} \sin^2\left(\frac{\Omega t}{2}\right). \tag{23}$$

In Fig. 18a, the color shows the behavior of the ground state population in a typical flux qubit (23) at various amplitudes of exposure [143]. Any single-qubit operation can be implemented if the conditions for the pulse parameters are satisfied: $A_\Omega \gg \omega_{01}$ and $\omega_{01}\tau \ll 1$. In this case, the 'leakage' to the second excited level $F = 1 - W_0 - W_1$ does not exceed 1% (Fig. 18b) in the considered ranges of pulse durations and amplitudes, which makes it possible to analyze the flux qubits within the two-level approximation.

4.4 Implementation of two-qubit operations using short unipolar pulses

Two-qubit operations in flux qubits can be implemented using a small (up to 2) number of short unipolar pulses. Consider this statement using an example of the simplest quantum register, consisting of two interacting qubits Q_1 and Q_2 [144]. The Hamiltonian of such a system is a tensor product of Hamiltonians of individual qubits $H^{(n)}$ $(n = 1, 2)$, determined by Eqn (5) in the two-level approximation, which is substantiated for a flux qubit with the term responsible for the interaction between two subsystems, H_{int}:

$$H(t) = H^{(1)}(t) \otimes I^{(2)} + I^{(1)} \otimes H^{(2)}(t) + H_{\text{int}}\,, \tag{24}$$

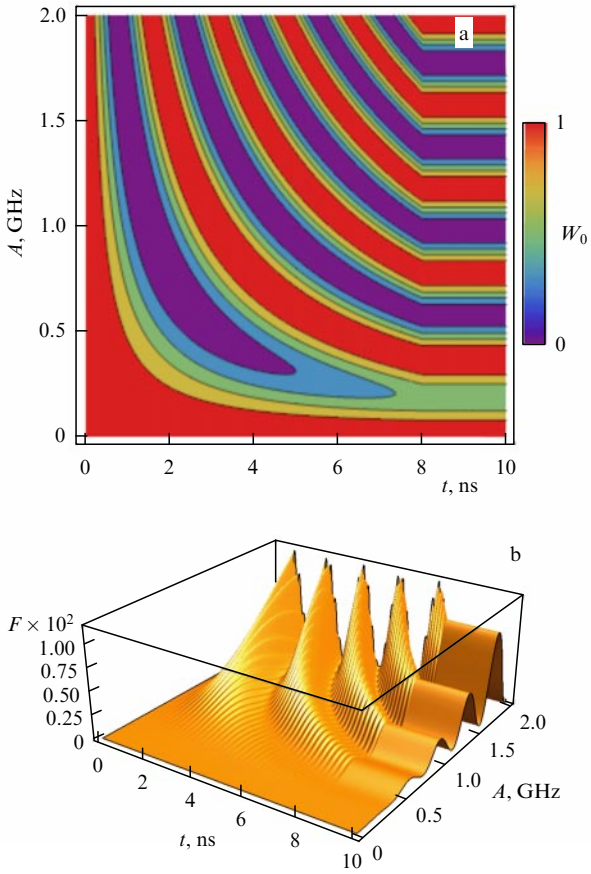

Figure 18. (Color online.) Dynamics of (a) the flux qubit ground state population and (b) leakage parameter F under the action of one unipolar pulse with $\tau = 8$ ns. Flux qubit parameters are taken from Ref. [143]: $\omega_{01}/(2\pi) = 0.3$ GHz and $\omega_{12}/(2\pi) = 28$ GHz. Color scale grades the variation of the ground state population.

where $I^{(n)}$ are unit matrices in the two-dimensional Hilbert space, and the term $H_{\text{int}} = J(t) = \sigma_x^{(1)} \otimes \sigma_x^{(2)}$ is responsible for the parametric tunable capacitive connection $J(t)$. Expression (24) can be presented in the matrix form

$$H(t) = -\frac{1}{2}\begin{vmatrix} \Delta_1 + \Delta_2 & \varepsilon_2(t) & \varepsilon_1(t) & J(t) \\ \varepsilon_2(t) & \Delta_1 - \Delta_2 & J(t) & \varepsilon_1(t) \\ \varepsilon_1(t) & J(t) & -\Delta_1 + \Delta_2 & \varepsilon_2(t) \\ J(t) & \varepsilon_1(t) & \varepsilon_2(t) & -\Delta_1 - \Delta_2 \end{vmatrix},$$

$$\varepsilon_n(t) = A_n \Theta(\tau_n - t)\Theta(t)\,, \qquad (25)$$

$$J(t) = J\Theta(\tau_J - t)\Theta(t)\,,$$

where Δ_n is the separation between the energy levels in the nth qubit $(n = 1, 2)$, A_n are the amplitudes of unipolar pulses $\varepsilon_n(t)$, $\tau_J = t_{\text{off},J} - t_{\text{in},J}$ is the duration of pulses $J(t)$ with the times of switching the exposure on $t_{\text{in},J}$ and off $t_{\text{off},J}$, and $\tau_n = t_{\text{off},n} - t_{\text{in},n}$ is the duration of pulses $\varepsilon_n(t)$ arriving at the nth qubit with the times of switching on $t_{\text{in},n}$ and off $t_{\text{off},n}$, respectively. In the absence of external action, it is convenient to present the state of a two-qubit system (25) in the computational basis [47]: $|\psi_1\rangle \otimes |\psi_2\rangle$, where $|\psi_{1,2}\rangle$ are the qubit wave functions in the form (6).

As an example, let us consider the implementation of quantum operations CNOT and SWAP using a pair of unipolar pulses. Assume that qubit Q_2 is in the ground state

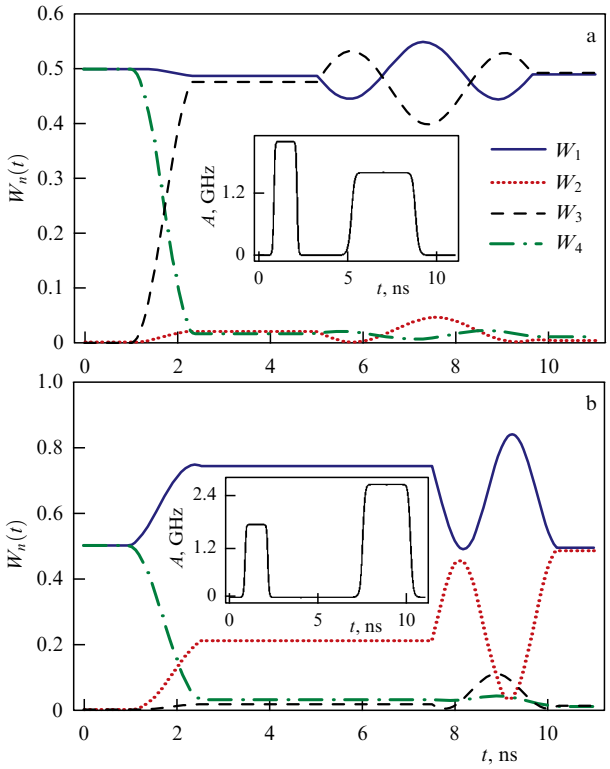

Figure 19. (Color online.) Dynamics of state populations $W_n(t)$ $(n = 1, 2, 3, 4)$ of a pair of coupled qubits in the process of executing CNOT (a) and SWAP (b) quantum operations. Parameters of unipolar pulses are shown in the insets; the qubit parameters are $\omega_{01}^{(1)}/(2\pi) = 0.05$ GHz, $\omega_{01}^{(2)}/(2\pi) = 0.07$ GHz, $J = 0.1$ GHz, $t_{\text{in},J} = 1$ ns; in Fig. a, $t_{\text{off},J} = 9.65$ ns, in Fig. b, $t_{\text{off},J} = 10.2$ ns.

$|\psi_2\rangle = |0\rangle$ and qubit Q_1 is initialized in the superposition state $|\psi_1\rangle = (1/\sqrt{2})(|0\rangle + |1\rangle)$ by means of a Hadamard gate.

The optimized choice of the unipolar action parameters $\varepsilon_n(t)$ and $J(t)$ allows obtaining the required probabilities of the transitions between the basis states of the two-qubit system with the populations $W_n(t)$ $(n = 1, 2, 3, 4)$. The implementation of two-qubit operations for flux qubits at time intervals ~ 10 ns [141, 144] is demonstrated for the CNOT operation in Fig. 19a and for the SWAP operation in Fig 19b. The accuracy of implementing two-qubit gates was 99%.

4.5 Implementation of a quantum algorithm using short unipolar pulses

Since we considered the fast execution of one- and two-qubit operations, it seems possible to realize a complete set of fast operations, using which any quantum algorithm can be reproduced as well.

One of the main quantum algorithms is Grover's search algorithm [47] of the optimal search for a unique argument x_0 of a Boolean function $f(x)$ of N variables, for which $f(x_0) = 1$. The complexity of executing the operations for a classical computer is $O(2^N)$. The quantum Grover algorithm allows a quadratic acceleration with the number of operations equal to $O(\sqrt{N})$.

Consider an implementation of Grover's algorithm using a two-qubit register of flux qubits Q_1 and Q_2 of the form (5). For this system, there are four basis states: $|x_n\rangle = |00\rangle$, $|01\rangle, |10\rangle, |11\rangle$, which define the set of definitions for $f(x)$. Let us describe step by step the evolution of the initial state

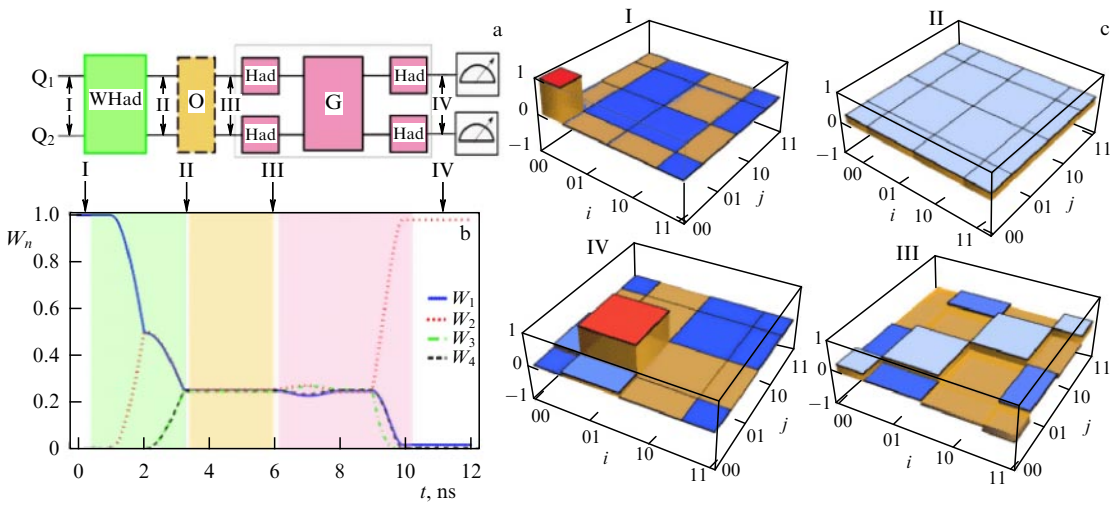

Figure 20. (Color online.) (a) Schematic of controlled evolution of two interacting qubits executing the Grover algorithm. (b) Time dependence of level populations in a two-qubit system under the action of unipolar pulses implementing the quantum Grover algorithm searching for a 'labeled' state $x_0 = |10\rangle$. Parameters of qubits and pulses are $\Delta_1 = 0.05$ GHz, $\Delta_2 = 0.07$ GHz; pulses acting on Q_1: $A_1 = 1.2$ GHz ($1 \leqslant t \leqslant 2.05$ ns), $A_1 = 1.6$ GHz ($6 \leqslant t \leqslant 7.92$ ns and $9 \leqslant t \leqslant 9.92$ ns); pulses acting on Q_2: $A_2 = 1.3$ GHz ($2.05 \leqslant t \leqslant 3.25$ ns), $A_2 = 1.6$ GHz ($6 \leqslant t \leqslant 7.92$ ns and $9 \leqslant t \leqslant 9.92$ ns); connection characteristics: $J = 0.01$ GHz ($1 \leqslant t \leqslant 3.25$ ns and $7.92 \leqslant t \leqslant 9$ ns); noise parameters: $\Gamma_{\phi,1}^{-1} = \Gamma_{\phi,2}^{-1} = 100$ μs. (c) Quantum tomography of the states of the density matrix real component $\mathrm{Re}\,[\rho_{ij}]$ at moments of time marked with arrows in panel b.

$|00\rangle$ (marked I in Fig. 20a, b) based on reconstructing its evolution by solving the equations for the density matrix $\mathrm{Re}\,[\rho]$ and its diagonal elements $W_n = \rho_{nn}$ (Fig. 20b).

Grover's algorithm consists of the following stages:

(1) the Walsh–Hadamard gate WHad (green block in Fig. 20a), a tensor product of single-qubit Hadamard operators that creates a superposition of all basis states with equal amplitudes ($W_n = 0.25$, mark II);

(2) the Oracle gate $O|x\rangle = (-1)^{f(x)}|x\rangle$ (yellow block in Fig. 20a) for 'marking' the state, e.g., $x_0 = |01\rangle$, which is reflected by the quantum phase of the state;

(3) the Grover diffusion gate (pink block in Fig. 20a) consisting of a sequence of three gates: Had, $\mathrm{G} = 2|\psi(0)\rangle\langle\psi(0)| - \mathrm{I}$, and Had.

Arrows and indexes I–IV in Fig. 20b show the moments of time at which the numerical reconstruction (tomography) of the quantum state displayed in Fig. 20c was carried out. The accuracy of the algorithm execution amounted to $F = \langle\psi|\rho|\psi\rangle = 93\%$. The obtained dependences agree with the data of the Grover algorithm implementation using superconducting qubits based on the Rabi technique [61].

5. Conclusion

Thus, the problem of controlling the state of a complex quantum system with configurable parameters of its elements and interconnections still has both fundamental and applied significance. Within the framework of this review, we analyzed the structure of individual qubits and the simplest quantum registers of superconducting quantum processors, paying particular attention to problems of controlling such systems. It was shown that the lifetime of quantum correlations in the system is fundamentally limited from above, whereas the duration of control actions within the traditional Rabi technique is limited from below.

The results of practical use of the described superconducting quantum processors at the time are seen to be both promising (the 'quantum supremacy' is demonstrated) and uncompleted (the achievement is obtained on a 'demonstration site'). Determining requirements for solving practically significant problems on quantum computers remains an issue of particular interest. Of course, in a general case, such problems can be solved by means of fault-tolerant quantum computers, in which the full-scale error correction codes are realized. However, the creation of such systems is seen as a matter in the fairly distant future. Nevertheless, some estimates can be made based on recent achievements in the field of quantum algorithms without complete correction. For example, for the quantum simulation of the two-dimensional Hubbard model using the variational method, 50 qubits must be involved, and then the quantum algorithm depth is estimated as 325 two-qubit operations [146, 147]. Therefore, we can conclude that, to achieve reasonable simulation accuracy, the relative errors of two-qubit operations must be much fewer than 10^{-3}, which is approximately two orders of magnitude lower than the present-day level. The presented estimates clearly substantiate the urgency of searching for fundamentally new solutions to increase the efficiency of the methods for controlling complex quantum systems.

The most promising search areas are either the reconstruction of the already used algorithms to adapt them to the specific features of the available elemental base (analog-digital method) or supplementing the elemental base to improve the efficiency of the existing algorithms. In the second case, there is an interesting approach to use superconducting digital circuits operating with classical data representation to make the processing of their I/O data as close to a 'quantum chip' as possible. Note that the operating principles of these logical devices based on the Josephson effect have already been reviewed in *Physics–Uspekhi* [145]. In the present review, we have shown that the pulses of current (or voltage) formed by Josephson digital circuits in control lines with subnanosecond duration allow implementing both the complete set of one- and two-qubit operations and the simplest quantum algorithms. In the future, this will allow increasing both the width and the depth of quantum circuits

at the expense of simplifying the control schemes and reducing the duration of key operations. However, note that studies devoted to searching for an optimal scheme of qubit control [148], increasing the transmon lifetime [149], or using alternative basic elements [150] have been intensely continued after this review was accepted for printing.

The authors are grateful to Yu E Lozovik, I A Rodionov, V S Stolyarov, and M Yu Kupriyanov for their fruitful discussions of the problems considered. The modeling of dynamic processes in quantum bits and the simplest registers was carried out with the support of the Russian Science Foundation (RSF) (grant no. 20-12-00130). The analysis of classical digital superconducting circuits was carried out with support from the President of RF (grant MD-186.2020.8). Access to scientific and technical literature was obtained due to support from the Interdisciplinary Research and Educational School of Lomonosov Moscow State University: Photonic and Quantum Technologies. Digital Medicine.

References

1. DiVincenzo D P *Fortschr. Phys.* **48** 9 (2000)
2. Dowling J P, Milburn G J *Philos. Trans. R. Soc. A* **361** 1809 (2003)
3. Ladd T et al. *Nature* **464** 7285 (2010)
4. Krantz P et al. *Appl. Phys. Rev.* **6** 2 (2019)
5. Kjaergaard M et al. *Annu. Rev. Condens. Matter Phys.* **11** 369 (2020)
6. Blatt J M, Weisskopf V F *Theoretical Nuclear Physics* (New York: Wiley, 1952); Translated into Russian: *Teoreticheskaya Yadernaya Fizika* (Moscow: IL, 1954)
7. Arute F et al. *Nature* **574** 505 (2019)
8. Clarke J, Wilhelm F K *Nature* **453** 1031 (2008)
9. Bouchiat V et al. *Phys. Scr.* **176** 165 (1998)
10. Nakamura Y, Pashkin Y A, Tsai J S *Nature* **398** 786 (1999)
11. Mooij J E et al. *Science* **285** 1036 (1999)
12. Chiorescu I et al. *Science* **299** 1869 (2003)
13. Martinis J M et al. *Phys. Rev. Lett.* **89** 117901 (2002)
14. Martinis J M *Quantum Inf. Process.* **8** 81 (2009)
15. Vion D et al. *Science* **296** 886 (2002)
16. Manucharyan V E et al. *Science* **326** 113 (2009)
17. Koch J et al. *Phys. Rev. A* **76** 042319 (2007)
18. Babu A P, Tuorila J, Ala-Nissila T *npj Quantum Inf.* **7** 30 (2021)
19. Park G et al. *J. Korean Phys. Soc.* **76** 1029 (2020)
20. Scully M O, Zubairy M S *Quantum Optics* (Cambridge: Cambridge Univ. Press, 1997); Translated into Russian: *Kvantovaya Optika* (Moscow: Fizmatlit, 2003)
21. Gisin N, Thew R *Nat. Photon.* **1** 165 (2007)
22. Kumar P et al. *Phys. Rev. Appl.* **6** 041001 (2016)
23. Hutchings M D et al. *Phys. Rev. Appl.* **8** 044003 (2017)
24. Yan F et al. *Nat. Commun.* **7** 12964 (2016)
25. Wang C et al. *Nat. Commun.* **5** 5836 (2014)
26. Gustavsson S et al. *Science* **354** 1573 (2016)
27. Riwar R et al. *Phys. Rev. B* **94** 104516 (2016)
28. Hosseinkhani A et al. *Phys. Rev. Appl. B* **8** 064028 (2017)
29. Vepsäläinen A P et al. *Nature* **584** 551 (2020)
30. Tanabashi M et al. *Phys. Rev. D* **98** 030001 (2018)
31. Martinis J M *npj Quantum Inf.* **7** 90 (2021)
32. Cardani L et al. *Nat. Commun.* **12** 2733 (2021)
33. Wilen C D et al. *Nature* **594** 369 (2021); arXiv:2012.06029
34. Braumüller J et al. *Appl. Phys. Lett.* **108** 032601 (2016)
35. Chow J M et al. *Proc. SPIE* **9500** 95001G (2015) Quantum Information and Computation XIII
36. Gambetta J M et al. *Quantum Inf.* **3** 2 (2017)
37. Abhinav K et al. *Nature* **567** 491 (2019)
38. Barends R et al. *Phys. Rev. Lett.* **111** 080502 (2013)
39. Versluis R et al. *Phys. Rev. Appl.* **8** 034021 (2017)
40. Anton S M et al. *Phys. Rev. Lett.* **110** 147002 (2013)
41. Bialczak R et al. *Phys. Rev. Lett.* **99** 187006 (2007)
42. Braumüller J et al. *Phys. Rev. Appl.* **13** 054079 (2020)
43. Zhang X et al. *Quantum Inf. Process.* **16** 309 (2017)
44. Shen Y et al. *Phys. Rev. A* **95** 020501 (2017)
45. Gong M et al. *Phys. Rev. Lett.* **122** 110501 (2019)
46. Rabi I *Phys. Rev.* **29** 174 (1927)
47. Nielsen M A, Chuang I L *Quantum Computation and Quantum Information* (Cambridge: Cambridge Univ. Press, 2000); Translated into Russian: *Kvantovye Vychisleniya i Kvantovaya Informatsiya* (Moscow: Mir, 2006)
48. McKay D C et al. *Phys. Rev. A* **96** 022330 (2017)
49. Jerger M et al. *Phys. Rev. Lett.* **123** 150501 (2019)
50. Chow J M et al. *Phys. Rev. A* **82** 040305 (2010)
51. Motzoi F et al. *Phys. Rev. Lett.* **103** 110501 (2009)
52. Martinis J M, Geller M R *Phys. Rev. A* **90** 022307 (2014)
53. Motzoi F, Wilhelm W K *Phys. Rev. A* **88** 062318 (2013)
54. McKay D et al. *Phys. Rev. A* **96** 101103 (2016)
55. Gambetta J M et al. *Phys. Rev. A* **83** 012308 (2011)
56. Abrams D M et al. *Phys. Rev. Appl.* **12** 064022 (2019)
57. Arrigo A D, Paladino E *New J. Phys.* **14** 053035 (2012)
58. Willsch D et al. *Phys. Rev. A* **96** 062302 (2017)
59. Werninghaus M et al. *npj Quantum Inf.* **7** 14 (2021)
60. Dewes A et al. *Phys. Rev. Lett.* **108** 057002 (2012)
61. DiCarlo L et al. *Nature* **460** 240 (2009)
62. Leek P J et al. *Phys. Rev. B* **79** 180511 (2009)
63. Corcoles A D et al. *Phys. Rev. A* **87** 030301 (2013)
64. Chow J M et al. *Phys. Rev. Lett.* **107** 080502 (2011)
65. Poletto S et al. *Phys. Rev. Lett.* **109** 240505 (2012)
66. Paik H et al. *Phys. Rev. Lett.* **117** 250502 (2016)
67. Chow J M et al. *New J. Phys.* **15** 115012 (2013)
68. Majer J et al. *Nature* **449** 443 (2007)
69. Strauch F W et al. *Phys. Rev. Lett.* **91** 167005 (2003)
70. Barends R et al. *Nature* **508** 500 (2014)
71. García-Ripoll J et al. *Phys. Rev. Appl.* **14** 044035 (2020)
72. Barron G S et al. *Phys. Rev. B* **101** 054508 (2020)
73. Hong Z P et al. *Phys. Rev. A* **97** 022332 (2018)
74. Egger D J et al. *Phys. Rev. Appl.* **11** 014017 (2019)
75. Yan T et al. *Phys. Rev. Lett.* **122** 080501 (2019)
76. Klots A, Ioffe L *Phys. Rev. B* **104** 144502 (2021)
77. Barends R et al. *Phys. Rev. Lett.* **123** 210501 (2019)
78. Abrams D M et al. *Nat. Electron.* **3** 744 (2020)
79. Rol M A et al. *Phys. Rev. Lett.* **123** 120502 (2019)
80. Chu J et al. *Phys. Rev. Appl.* **13** 064012 (2020)
81. Zheng S B, Guo G C *Phys. Rev. Lett.* **85** 2392 (2000)
82. Chen Y et al. *Phys. Rev. Lett.* **113** 220502 (2014)
83. Neill C J "A path towards quantum supremacy with superconducting qubits", Ph.D. Thesis (Santa Barbara, CA: Univ. of California, 2017)
84. Yan F et al. *Phys. Rev. Appl.* **10** 054062 (2018)
85. Zulehner A, Wille R, in *Proc. of the 24th Asia and South Pacific Design Automation Conf., ASP-DAC 2019, Jan. 21–24, 2019, Tokyo, Japan* (2019) p. 185
86. Wang Y et al. *Quantum Inf.* **4** 46 (2018)
87. Ozaeta A, McMahon P *Quantum Sci. Technol.* **4** 2 (2019)
88. Zulenher A et al. *IEEE Trans. Comput. Aid. D* **38** 1226 (2018)
89. Narendra N et al., arXiv:1712.07326
90. Ferrari D, Amoretti A *Int. J. Quantum Inf.* **16** 1840006 (2018)
91. Singh R K et al., arXiv:1807.02883
92. Li G et al., in *ASPLOS '19: Proc. of the Twenty-Fourth Intern. Conf. on Architectural Support for Programming Languages and Operating Systems, April 2019*, p. 1001, https://doi.org/10.1145/3297858.3304023
93. Nishio S et al. *ACM J. Emerging Technol. Comput. Syst.* **16** (3) 32 (2020)
94. McCaskey A J et al. *npj Quantum Inf.* **5** 99 (2019)
95. Reagor M et al. *Sci. Adv.* **4** aao3603 (2018)
96. Li A C Y et al. *APS March Meeting* K42.005 (2019)
97. Johnson B et al. *APS March Meeting* K33.001 (2018)
98. Hartung T, Jansen K *J. Math. Phys.* **60** 093504 (2019)
99. Lamm H, Lawrence S *Phys. Rev. Lett.* **121** 170501 (2018)
100. Olivares-Sánchez J et al. *Quantum Rep.* **2** 293 (2020)
101. Otterbach J S et al., arXiv:1712.05771
102. Zhao Z et al. *Quantum Mach. Intell.* **1** 41 (2019)
103. Dumitrescu E F et al. *Phys. Rev. Lett.* **120** 210501 (2018)
104. Fingerhuth M, Babej T, Ing C, arXiv:1810.13411
105. Wootton J R, arXiv:1806.02736
106. Google AI Quantum and Collab., Arute F et al. *Science* **369** 1084 (2020)

107. Harrigan M P et al. *Nat. Phys.* **17** 332 (2021)
108. Benjamin S, Bose S *Phys. Rev. Lett.* **90** 247901 (2003)
109. Martin A et al. *Phys. Rev. Res.* **2** 013012 (2020)
110. Xu K et al. *Phys. Rev. Lett.* **120** 050507 (2018)
111. Smith J et al. *Nat. Phys.* **12** 907 (2016)
112. Jurcevic P et al. *Nature* **511** 202 (2014)
113. Babukhin D V et al. *Phys. Rev. A* **101** 052337 (2020)
114. McDermott R et al. *Quantum Sci. Technol.* **3** 024004 (2018)
115. Likharev K K, Semenov V K *IEEE Trans. Appl. Supercond.* **1** 3 (1991)
116. Zhou X et al. *IEEE Trans. Appl. Supercond.* **11** 1018 (2001)
117. Crankshaw D S et al. *IEEE Trans. Appl. Supercond.* **13** 966 (2003)
118. Semenov V K et al. *IEEE Trans. Appl. Supercond.* **13** 960 (2003)
119. Likharev K K *Radio Eng. Electron. Phys.* **19** 109 (1974); *Radiotekh. Elektron.* **19** 1494 (1974)
120. Shapiro S, Janus A R, Holly S *Rev. Mod. Phys.* **36** 223 (1964)
121. Kaplunenko V K et al. *IEEE Trans. Magn.* **25** 861 (1989)
122. Bastrakova M V et al. *Supercond. Sci. Technol.* **35** 055003 (2022)
123. Rylyakov A, http://www.physics.sunysb.edu/Physics/RSFQ/Lib/AR/dcsfq.html
124. Whiteley S R *IEEE Trans. Magn.* **27** 2902 (1991)
125. McDermott R, Vavilov M G *Phys. Rev. Appl.* **2** 014007 (2014)
126. Liebermann J, Wilhelm F K *Phys. Rev. Appl.* **2** 024022 (2016)
127. Li K et al. *Phys. Rev. Appl.* **12** 014044 (2019)
128. Leonard E et al. *Phys. Rev. Appl.* **11** 014009 (2019)
129. Bodenhausen G, Freeman R, Morris G A *J. Magn. Reson.* **23** 171 (1976)
130. Morris G A, Freeman R *J. Magn. Reson.* **29** 433 (1978)
131. Patel U et al. *Phys. Rev. B* **96** 220501 (2017)
132. Arkhipov R M et al. *Opt. Lett.* **44** 1202 (2019)
133. Arkhipov R et al. *Opt. Express* **28** 17020 (2020)
134. Popolitova D V et al. *Beilstein J. Nanotechnol.* **10** 1548 (2019)
135. Soloviev I I et al. *Phys. Rev. B* **92** 014516 (2015)
136. Soloviev I I et al. *Appl. Phys. Lett.* **105** 202602 (2014)
137. Soloviev I I et al. *Phys. Rev. E* **87** 060901 (2013)
138. Klenov N V et al. *Phys. Solid State* **52** 11 (2010)
139. Denisenko M V, Klenov N V, Satanin A M *J. Phys. Conf. Ser.* **955** 1 012004 (2018)
140. Denisenko M V et al. *AIP Conf. Proc.* **1936** 020009 (2018)
141. Bastrakova M V, Klenov N V, Satanin A M *Phys. Solid State* **61** 1515 (2019); *Fiz. Tverd. Tela* **61** 1565 (2019)
142. Klenov N V et al. *Beilstein J. Nanotechnol.* **6** 1946 (2015)
143. Tao W et al. *Chin. Phys. Lett.* **23** 971 (2006)
144. Bastrakova M V, Klenov N V, Satanin A M *J. Exp. Theor. Phys.* **131** 507 (2020); *Zh. Eksp. Teor. Fiz.* **158** 579 (2020)
145. Likharev K K *Sov. Phys. Usp.* **26** 87 (1983); *Usp. Fiz. Nauk* **139** 169 (1983)
146. Cade C et al. *Phys. Rev. B* **102** 235122 (2020)
147. Fedorov G P et al. *Phys. Rev. Lett.* **126** 180503 (2021)
148. Gong M et al. *Science* **372** 948 (2021)
149. Wang C et al., arXiv:2105.09890
150. Nguyen L B et al., arXiv:2201.09374